DPG - FRÜHJAHRSTAGUNG

(Düsseldorf, FRG, Feb 29 - Mar 4, 1988)

IPP III/134 April 1988

MAX-PLANCK-INSTITUT FÜR PLASMAPHYSIK

8046 GARCHING BEI MÜNCHEN

DPG - FRÜHJAHRSTAGUNG

(Düsseldorf, FRG, Feb 29 - Mar 4, 1988)

IPP III/134 April 1988

ASDEX CONTRIBUTIONS TO THE DPG FRÜHJAHRSTAGUNG

(Düsseldorf, 29.2.-4.3.1988)

Charge Exchange Spectroscopy (CXRS)
of highly ionized Ions in ASDEX

J. V. HOFMANN, G. FUSSMANN, G. JANESCHITZ

Max-Planck-Institut für Plasmaphysik
D-8046 Garching

ABSTRACT

We report on measurements of visible transitions from highly ionized krypton and sulfur and compare them with calculations.

1. Introduction

In large Tokamak devices like ASDEX light impurities - in particular carbon or oxygen, which are always present - are totally stripped in the inner part of the plasma and even medium Z impurities like chromium, iron, nickel or copper are highly ionized. Charge exchange recombination (CXR) can then be an important energy loss mechanism in neutral beam heated plasmas due to enhanced radiation after the charge capture process. On the other hand, CXR provides a mean to study fully stripped ions in the plasma core and to deduce general information about the plasma, like ion temperature, plasma rotation velocity or impurity concentrations.

To observe the transitions resulting from CXR a sufficiently high density of high energy H-neutrals is needed which can be provided by neutral heating or diagnostic beams. Due to the very strong dependence of the reaction rates for CX-recombination into levels of high quantum states n with respect to the neutral particle energy, (R.J.Fonck et al.[1]), the contribution of the beam halo particles is negligible when corresponding $\Delta n = 1$ transitions are measured.

The very close coupling of the signals to the beam particle flux, (P.J.Carolan et al.[2]), allows direct identification of the lines.

During neutral beam injection into Tokamak discharges CXR is the dominating recombination process and the cross sections for the electron transfer reaction are of the order of 10^{-15} cm^2. The basic reaction is:

$$\begin{aligned} \mathbf{H}^0_{(Beam)} + \mathbf{X}^{q+}_{(Impur.)} &\rightarrow \mathbf{H}^+ + \mathbf{X}^{(q-1)+}(n,l)^* \\ &\rightarrow \mathbf{H}^+ + \mathbf{X}^{(q-1)+}(n',l')^* + h\nu \end{aligned} \tag{1.1}$$

Due to conservation of energy and angular momentum of the exchanged electron a resonance character in the reaction is observed. This gives rise to the population of highly excited Rydberg states $X^{(q-1)+}(n,l)^*$; the preferentially populated levels can be estimated via $n_{res} \simeq Z^{3/4}$ and $l_{res} = n_{res}$-1. The decay of the levels with maximum angular momentum l = n-1 takes place solely via $\Delta n = 1$ transitions, refered to as Y-RAST transitions. These are of particular importance for the resonant level n_{res}. *(Fig. 1)*

Since the cross sections scale approximately proportional to Z one may use high Z impurities for specific meassurements. Because the transition propabilities are strongly dependent on Z and n, $A_n \sim Z^4 / n^\alpha$ with α = 3-5 (H. A. Bethe et al.[3], I. I. Sobelman et al.[4]), even for high n very short lifetimes generally result.

Great interest arose in the investigation of transitions in the visible range of the spectrum first of all because of easy experimental application and the flexibility in using fibers. A further advantage is the easy identification of the lines due to their large width according to doppler broadening which is the dominating mechanism in this region.

In the visible range, however, the corresponding main quantum numbers n are well above the resonant one (n_{res}) and the cross sections for population of these high n levels and the resulting intensities of the observed lines are thus of great importance. Our preliminary studies already reveal a much stronger decay in intensities and cross sections than the n^{-3} dependance found for low n levels and which was asumed to hold for the high n states, too, (P.J.Carolan et al.[2]).

In this paper we present experimental data for sulfur and krypton which confirm a very rapid decay of line intensity with n (near exponential).

2. Population structure and rate coefficients

In order to calculate the population of excited and ground states, atomic data for the CXR, the cascading processes and the l-mixing collisions are needed.

Because of lack of such data, especially for high and medium Z-elements our calculations are restricted to H-like systems and we choose H-like oxygen as a first example.

In the following we use the line intensity of the O VIII - transition n = 10 - 9 ($\lambda =$ 606.8 nm), measured in an ASDEX discharge (# 20070, with 3.3 MW of neutral beam injection) as input for a code by H.P.Summers[5]. We calculate the rate coefficients for the population of different n levels by CXR and the resulting effective rates. The effective rate coefficient introduced here reflects all processes leading to a transition observed in CXRS. These are the level population due to the primary CXR-process, the change of this population due to cascading and l-mixing collisions and the resulting emission.

The relation between the observed intensity along a line of sight through the plasma I_{ik}^{cx}, the primary CXR-rate R_k^{cx} for population of level k and the effective rate $< \sigma v >_{ik}^{eff}$ is given by

$$I_{ik}^{cx} = \int A_{ik}^{(Z-1)+} N_k^{(Z-1)+} \, dl \tag{2.1}$$

$$= \int N_H N^{Z+} < \sigma v >_{ik}^{eff} \, dl \tag{2.2}$$

with $N_k^{(Z-1)+}$ being the population density of level k, $A_{ik}^{(Z-1)+}$ the Einstein coefficient for transition k-i, N_H the density of fast neutral hydrogen atoms and N^{Z+} the density of the fully ionized species. Equation (2.2) is actually the definition of $< \sigma v >^{eff}$. Neglecting collisions, the density $N_k^{(Z-1)+}$ is determined by the rate equation

$$\frac{dN_k^{(Z-1)+}}{dt} = N_H N^{Z+} R_k^{cx} + \sum_{j>k} A_{kj}^{(Z-1)+} N_j^{(Z-1)+} - \sum_{j<k} A_{jk}^{(Z-1)+} N_k^{(Z-1)+} = 0 \qquad (2.3)$$

Resolving for $N_k^{(Z-1)+}$ we obtain for steady state

$$N_k^{(Z-1)+} = \left(N_H N^{Z+} R_k^{cx} + \sum_{j>k} A_{kj}^{(Z-1)+} N_j^{(Z-1)+} \right) A_k^{-1} \qquad (2.4)$$

$$A_k = \sum_{j<k} A_{jk}^{(Z-1)+} \qquad (2.5)$$

which may be solved by downward recursion starting at a maximum level N_{max}. The effective rate is then given by

$$< \sigma v >_{ik}^{eff} = \left(R_k^{cx} + \sum_{j>k} A_{kj}^{(Z-1)+} \frac{N_j^{(Z-1)+}}{N_H N^{Z+}} \right) A_k^{-1} A_{ik}^{(Z-1)+} \qquad (2.6)$$

In order to connect the evaluated population densities of the excited states of $O^{(Z-1)+}$ to its ground state population and the population of the fully ionized species O^{Z+} we determined the ratio of these two densities from the ionisation and recombination rates averaged over flux surfaces in the torus using a transport code, (G.Janeschitz et al.[6]), which solves the equation

$$\frac{dN^{Z+}}{dt} = N_e N^{(Z-1)+} S^{Z-1} - N_e N^{Z+} R_{\nu+d}^{Z} - N_H N^{Z+} R_{cx}^{Z} - div(\overrightarrow{\Gamma^{Z+}}) = 0 \qquad (2.7)$$

as a function of radius r in cylindrical geometry. Ignoring the transport term $div(\overrightarrow{\Gamma^{Z+}})$, the so called corona equilibrium

$$\frac{N^{(Z-1)+}}{N^{Z+}} = \frac{R_{\nu+d}^{Z} + \frac{N_H}{N_e} R_{cx}^{Z}}{S^{Z-1}} \qquad (2.8)$$

is obtained, which in the present case includes CX-recombination (R^Z_{cx}) in addition to radiative and dielectronic recombination ($R^Z_{\nu+d}$). The neutral density N_H in equation (2.8) becomes also a function of r when averaged over flux surfaces. This quantity is obtained by envoking a beam absorbtion code, (F.P.Penningsfeld[7]). The levels and the corresponding rates are shown in *(Fig. 2)*.

Our main interrest is the n-dependence of the primary CX-rates and the resulting effective rates at high n well above n_{res}. As to be seen from *(Fig. 3)* an almost exponential decay is prevailing in this range.

3. Measurements in ASDEX

To allow systematic studies of these high n levels we choose krypton and sulfur which where added during the discharge by gaspuffing (in the case of sulfur as H_2S). In the visible and UV range of the spectrum all Δn = 1 transitions of the Li-like sulfur $^{16}S^{13+}$ (5 lines) and the Na-like krypton $^{36}Kr^{25+}$ (8 lines) could be identified and the observed wavelengths agreed very well with those calculated for corresponding H-like ions. Low l-state transitions (i.e. $l \ll n-1$) which should produce well separated satellites could not be substantiated.

The observed intensities show in both cases a strong decay towards higher main quantum numbers n and apart from the lowest and highest n-value the data indicate an exponential decay *(Fig. 4)*. So far this result is preliminary since the calibration of the spectrometer and the optical transmission line has to be confirmed by an updating measurement especially in the high wavelength range.

Additional CXR-atomic data for the Li- and Na-like systems are needed for more specific calculations on these systems and to allow the proper comparison with our measurements.

4. Summary

- **CXRS enables measurements of fully stripped Ions. Specially in the visible range it provides a convenient mean for impurity identification and absolute concentration measurements.**
- **For H-like oxygen the atomic level population was calculated and a comparison between the primary CXR-rates and the resulting effective rates has been performed. This indicates an exponential decay both for the primary and the effective rates.**
- **We measured Li-like sulfur and Na-like krypton transitions in the visible range and observed a strong decrease of the intensities for higher n.**
- **To work out effective and primary rate coefficients and to perform a proper comparison to our measurements for these systems more atomic data for l-resolved CXR into high quantum states and for collision rates between these states for Li- and Na-like systems are needed.**

REFERENCES

1. R. J. Fonck, D. S. Darrow, K. P. Jaehnig, Phys. Rev. A, Vol. 29 No.6, 3288 (1984)
2. P. G. Carolan, B. P. Duval, A. R. Field, S. J. Fielding, N. C. Peacock, G. Fußmann, G. Janeschitz, J. Hofmann, K. Behringer, R. C. Isler, Phys. Rev. A, Vol 35, 3454 (1987)
3. H. A. Bethe, E. E. Salpeter, Quantum Mechanics of one and two Electron Atoms, Springer, Berlin 1957, p 268 ff
4. I. I. Sobelman, L. A. Vainshtein, E. A. Yukov, Excitation of Atomas and Broadening of Spectral Lines, Springer, Berlin 1981, p 142 ff
5. J. Spence, H. P. Summers, J. Phys. B Vol 19, 3749 (1986)
6. G. Fußmann, G. Janeschitz, K. Krieger, private communication
7. F. P. Penningsfeld, IPP - Report 4/229, (1986)

Figure captions

Fig. 1: Level and cascade diagram for H-like oxygen O^{7+}: The cascade on the left are the resonance transitions of the Lyman series; the series shown in the middle is an example of the most propable one between high n, $l = 5$ states ($n,l \rightarrow n' = l$, $l' = l\text{-}1$); hatched circle: resonant levels predominantly populated by CXR; hatched ellipse: visible and UV region; hatched arrows: Y-RAST transitions.

Fig. 2: Diagram illustrating O^{7+} and O^{8+} levels and connecting rates: Left: connection of O^{7+} ground state with the O^{8+} sate by ionisation and recombination rates. Right: population and cascades for the excited levels of O^{7+}.

Fig. 3: Comparison of calculated primary rate coefficients for population of O^{7+} by CXR and the calculated effective rate coefficients after cascading, mixing and Δ n = 1 transitions. The primary rate is seen to show a prominent resonance at $n \approx 5$ while this feature is smeared out in the effective rate by cascading, mixing collisions and transitions. Both rates show an exponential like decay above $n_{res} = 5$.

Fig. 4: Measured intensities for $\Delta n = 1$ transitions of Na-like ${}^{36}Kr^{25+}$ well above n_{res} = 11. Apart from the lowest and highest n-values the data may be roughly approximated by an exponential law (solid line).

Spectroscopic measurement of the ion temperature on ASDEX

P. Lee+, R. Nolte, ASDEX-Team, NI-Team

IPP Garching, EURATOM Association
+GA Technologies, San Diego

In the center of Tokamak discharges impurity ions are in He- or Li- like ionisation stages over a broad range of temperatures (0.5 - 10 keV). The spectral lines of these ions are lying in the SX-ray region (1 – 10Å). In this region highly resolving crystall spectrometers can be used. Therefore one important application of SX-ray spectroscopy is the measurement of the ion temperature from doppler broadening. This requires a spectrometer with a resolution $\lambda/\Delta\lambda > 3000$ for typical medium weight impurity ions.

On ASDEX a medium size curved crystall spectrometer in Johann mounting is avialable for SX-ray spectroscopy. The instrument is characterized by:

- diameter of the rowland circle: 1500mm
- active crystall area: 50mm × 10mm
- detector: position sensitive proportional counter

Several effects contribute to the instrumental width of the spectrometer:

(numbers corresponding to the resonance line of ClXVI at $\lambda = 4.4442$Å)

- geometrical broadening(31%)
- detector resolution(43%)
- imperfect curvature of the crystalls (26%)

An important reduction of the effects of imperfect curvature has been achieved by using new high quality crystall holders which have been manufactured at the Los Alamos National Laboratory. For testing the optical quality of the holders the image of a pointlike light source in a rowland like geometry ($\Theta_B = 85°$) has been recorded$^{1)}$. Examples of these traces for several old and new holders are given in fig. 1. With the new holders a resolving power $\lambda/\Delta\lambda = 5000$ has been reached.

The instrument can be scanned in poloidal direction from $r/a = -0.85$ up to $r/a = +0.05$ thus allowing spatially resolved measurements. The line of sight of the Johann spectrometer crosses the neutral particle beam. Therefore contributions from charge exchange recombination to the population of the levels of He-like ions can be expected.

As first modelling calculations show this could explain the broad emission profiles of the resonance lines of SVI and ClXVI which have been found during beam heated ASDEX discharges$^{2)}$. A direct signature for the contribution of charge exchange from fast beam neutrals could be obtained from the spectra of highly excited He-like ions. Charge exchange predominantly populates levels with the resonant quantum numbers n=8,9 which would produce a deviation from the n^{-3}-dependence of the intensity expected for pure impact excitation of these levels. For $r/a > -0.55$ such deviations could not be observed. In fig. 2 spectra of transtions from highly excited states to the ground state of ArXVII are shown for two radial positions. The situation can be clarified by measurements on outer flux surfaces for which the contribution of charge exchange should be most important.

For medium Z impurity ions like SXV or ClXVI the experimentally observed line width is dominated by Doppler broadening. On the other hand these impurities are naturally occuring in ASDEX discharges ($\simeq 10^{-4} n_e$). They are thus well suited for a passive measurement of the ion temperature.

For a Maxwellian velocity distribution the experimental line profile $I(\omega)$ reads:

$$I(\omega) = \int\int f_a(\omega - \omega') e^{-(\frac{\omega' - \omega''}{\Delta\omega_D})} I_n(\omega'') d\omega'' d\omega'$$

$f_a(\omega)$: instrumental profile

$I_n(\omega)$: natural line profile

$\Delta\omega_D$: Doppler width

For the measurements which are presented here the $1s^2 - 1s2p$ resonance line of ClXVI has been used. The contributions to the total width of this line are:

- instrumental width: $\Delta\lambda_I = 0.49$mÅ
- natural line width: $\Delta\lambda_n = 0.09$mÅ
- Doppler width: $\Delta\lambda_D = 1.82\text{mÅ}\sqrt{T_i/\text{keV}}$

With the exception of some minor structures in the outer line wings which are due to deviations of the instrumental profiles from a gaussian the experimental line profiles could be fitted by a single gaussian. Fig.3 shows a gaussian fit to a line profile measured during the beam heated phase of a discharge. For comparison a gaussian with the instrumental width is included. To avoid systematic errors from unresolved dielectronic satellites ($n > 3$)

only a very small part of the long wavelength wing has been used for this fit. This difficulty can be avoided by using the $1s^2 - 1s3p$ transition for which no unresolved satellites are known. On the other hand this line is weaker than the resonance line normally.

Preliminarily the instrumental profile has been estimated from measurements at great radial distances from the plasma center (r/a = 0.75). The ion temperature at this position was 0.25(5) keV. A direct measurement of the instrumental profile with a special x-ray tube will be made in future.

The ion temperatures measured so far are systematically lower by 20% than the results of the ASDEX neutral particle analysis (NPA). Typical results are displayed in fig. 4. These deviations can probably be attributed to the influence of line integration over the broad emission profiles. They can be corrected if experimental emission profiles are avialable.

References:

[1] P. Lee, R. Nolte IPP Report III/127, Garching 1987

[2] P. Lee, R. Nolte, G. Fussmann and G. Janeschitz, invited paper: Conference on Atomic Processes in Plasma, Santa Fee 1987

Figure captions:

Fig. 1: Focal plane image of a pointlike light source for three crystall holders.

Fig. 2: Spectra of ground state transitions from highly excited states of ArXVII for two radial positions. The n=5 line is lowered by vignetting.

Fig. 3: Profile of the ClXVII resonace line during neutral beam heating. The solid line is a gaussian fit to the experimental data. The dashed line indicates the instrumental profile. The region used for the fit is marked by arrows.

Fig. 4: Ion temperatures from crystall spectroscopy (X-tal) and neutral particle analysis (NPA)for a beam heated discharge.

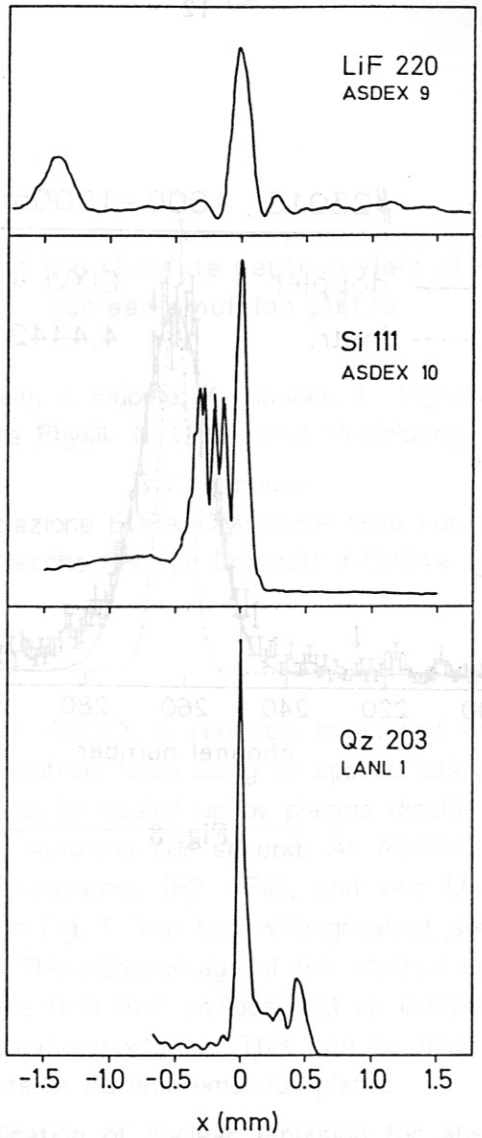
LiF 220
ASDEX 9
Si 111
ASDEX 10
Qz 203
LANL 1
-1.5
-1.0
-0.5
0
0.5
1.0
1.5
x (mm)

Fig. 1

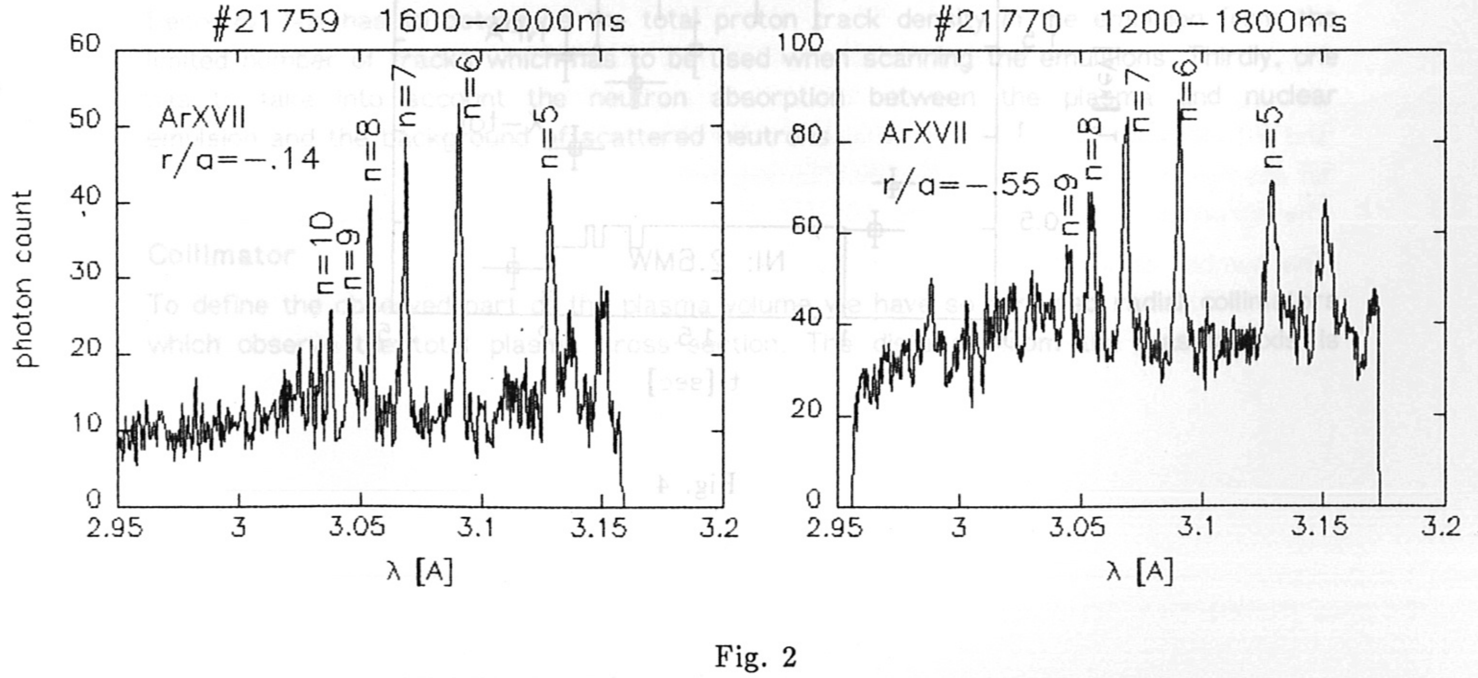
#21759 1600–2000ms
ArXVII
r/a=-.14
n=10
n=9
n=8
n=7
n=6
n=5
photon count
0
10
20
30
40
50
60
2.95
3
3.05
3.1
3.15
3.2
λ [A]
#21770 1200–1800ms
ArXVII
r/a=-.55
n=9
n=8
n=7
n=6
n=5
0
20
40
60
80
100
2.95
3
3.05
3.1
3.15
3.2
λ [A]

Fig. 2

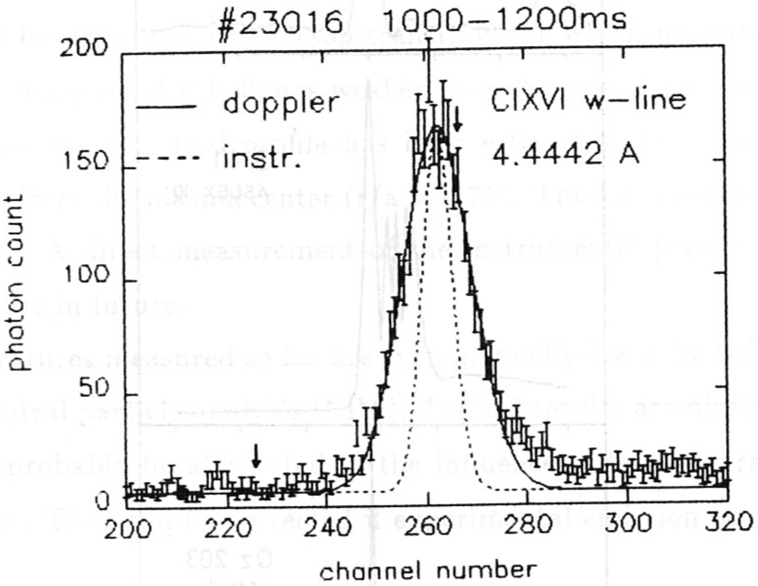
#23016 1000–1200ms
doppler
instr.
ClXVI w-line
4.4442 A
photon count
0
50
100
150
200
200
220
240
260
280
300
320
channel number

Fig. 3

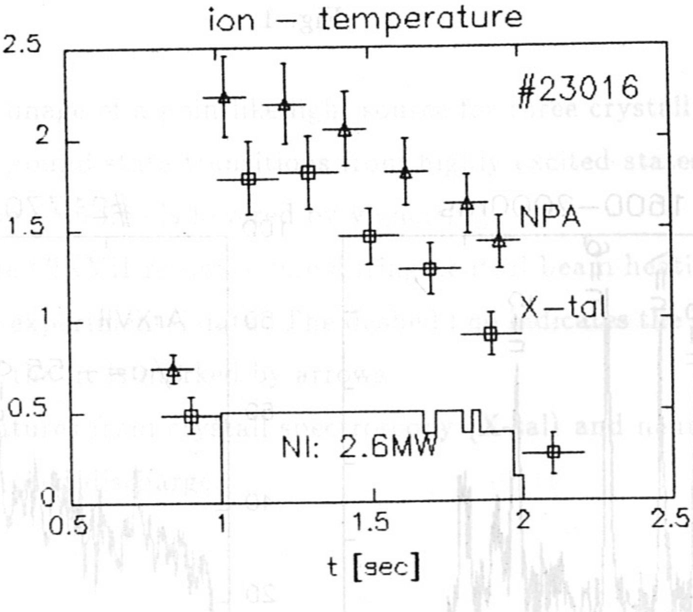
ion – temperature
#23016
NPA
X-tal
NI: 2.6MW
T_i [keV]
0
0.5
1
1.5
2
2.5
0.5
1
1.5
2
2.5
t [sec]

Fig. 4

Measurement of the absolute neutron yield of ASDEX with nuclear emulsion plates

R. Klein, J. Hubele, K. Hübner, L. Ingrosso
Institut für Angewandte Physik II, Universität Heidelberg, D-6900 Heidelberg
B.V. Robouch
Associazione EURATOM-ENEA sulla Fusione
Centro Ricerche Energie Frascati, I-00044 Frascati

Introduction

The absolute neutron rate of ASDEX is routinely measured with BF_3- and U-counters which are calibrated at low neutron rates using an appropriate neutron source inside the vessel, and these then have to be scaled up by plasma discharges for the total interval of interest from 10^9 to 10^{15} neutrons per second. At ASDEX we use an array of one ^{3}He-counter (F1), three BF_3-counters (F2 - F4), and two U-counters (F5, F6). Their effective ranges are shown in Fig. 1. The two with greatest sensitivities (Eich 1, Eich 2) are calibrated absolutely [1]. The disadvantage of this method is an increasing calibration error for higher neutron yields It is thus obvious that an independent absolute calibration check at high yields is of great importance. This can be done by a yield determination using activation measurements or nuclear emulsion plates.

This paper reports the application of nuclear emulsion for absolute yield determination. Nuclear emulsion plates measure the time-integrated neutron fluence at the position of their exposure. For ASDEX they are useful at neutron rates in the range from 10^{11} to 10^{15}n/s, depending on the number of discharges available.

When emulsions are used, three problems have to be solved. Firstly, one has to determine the observed part of the plasma to scale it to the total plasma volume. Secondly, one has to determine the total proton track density in the emulsion from the limited number of tracks which has to be used when scanning the emulsions. Thirdly, one has to take into account the neutron absorption between the plasma and nuclear emulsion and the background of scattered neutrons.

Collimator

To define the observed part of the plasma volume we have so far used radial collimators which observe the total plasma cross-section. The distance from the plasma axis is chosen in such a way that the observed neutron fluence is not noticeably affected by the radial distribution of the neutron source in the plasma. Fig. 2 gives a schematic vertical cut through the arrangement of plasma and collimator.

The use of collimators has two other advantages. Firstly, the background of collided neutron flux which would otherwise enter the emulsion from all sides, is essentially reduced. Secondly, to a certain degree a direction of incidence of the neutrons is defined, and thus a direct determination of the neutron energy spectra by the emulsion becomes possible.

Nuclear emulsion

In the nuclear emulsion the neutrons are detected by the tracks of recoiled protons. The proton energy is deterimined by $E_p = E_n \cos^2\Theta$. Here E_n is the energy of the neutron and Θ the scattering angle, i.e. the angle between the direction of incidence of the neutron and the proton track. With increasing scattering angle Θ the proton energy and thus the track length become very small. For this reasons and because of some problems in measuring large scattering angles, the scanning of tracks is limited to not too large angles Θ, usually to 20^0 or 30^0.

First of all, extrapolation to $\Theta = 90^0$ is necessary. This is done by fitting the measured integral track distributions to the theoretical ones. We use not only the distribution over Θ but also that over the so-called depth angle Ψ (angle between the track and its projection into the plane of the emulsion) and plane angle Φ (angle between the track projection and the central line of incidence of the neutrons). These different angles are illustrated in Fig. 3. The theoretical track distributions are given by

$$P(\Theta) = P_{90^o} \sin^2\Theta, \qquad (1)$$

$$P(\Phi) = P_{90^o} \frac{2}{\pi} \sin\Psi_{max} (\Phi + \frac{1}{2} \sin 2\Phi), \qquad (2)$$

$$P(\Psi) = P_{90^o} \frac{2}{\pi} (\Phi_{max} + \frac{1}{2} \sin 2\Phi_{max}) \sin\Psi. \qquad (3)$$

P_{90^o} is the total number of tracks which has to be determined. These integrated distributions determine the number tracks with angles smaller than Θ (1), smaller than Φ and a fixed value Ψ_{max} (2), or smaller than Ψ and a fixed value Φ_{max} (3) . Fig. 4 gives an example of a measured track distribution over Ψ (crosses) and the corresponding fit. The agreement is excellent up to 40^0, which was the scanning limit in this case.

The number of scattered protons must be further corrected for protons that leave the emulsion. Additionally, one has to expect a small change in the theoretical distributions caused by the spread in the angles of incidence of the neutrons. Both corrections together are only of the order of 2 - 3%. More serious is the fact that there are tracks wich are so strongly curved or bent that it is not possible to measure their scattering angle. These tracks are simply counted; they lead to a correction of the order of 30%.

From the total track number the neutron fluence at the emulsion is calculated by

$$\Phi_n = P_{90^o} / A\,\varepsilon. \qquad (4)$$

Here A is the area of the emulsion and ε its sensitivity (tracks per neutron) where n_p is

$$\varepsilon = \overline{\sigma_{np}}\, n_p\, d, \qquad (5)$$

the proton density of the emulsion and d its thickness. The mean neutron-proton cross-section for the considered range of the neutron energy spectrum n(E) is determined by

$$\overline{\sigma_{np}} = \int n(E)\, \sigma_{np}(E)\, dE. \qquad (6)$$

The efficency ε has a typical value of 1/610 recoiled protons per incoming neutron.

Neuton absorption and scattering

The total neutron yield of a discharge is related to the neutron fluence at the position of the emulsion by

$$Y = \Phi_n / F. \qquad (7)$$

By this definition the fluence factor F contains several effects; firstly, the ratio of observed to total plasma volume; secondly, the decrease of neutron fluence with the square of the distance between the plasma and emulsion; thirdly, the absorption in the material between the plasma and emulsion; fourthly, the background of scattered neutrons. For ASDEX we determine all these corrections by numerical calculations using the VINIA software [2].

Errors

An essential problem in absolute measurements are the errors introduced in the procedure. Here we have to consider the errors of the total track number P_{90^o}, of the proton density n_p and the thickness d of the emulsion, and of the fluence factor F. Most important are the errors in n_p and d because both are given by the producer with an accuracy of only 5 to 10%. The error in P_{90^o} depends mainly on the accuracy of the scanning procedure and the total number of tracks used. An error of less than 5% seems to be achievable.

It is possible to reduce the statistical error of the numerical determination of the fluence factor to about 2 to 3%. For ASDEX the correction for scattered neutrons, which is contained in F, is of the order of 30 to 50% in the cases of collimators observing the total plasma cross-section. VINIA calculations (Fig. 5) demonstrated that the apparent emission profile of the scattered neutron as seen by the emulsion inside the collimator is much broader than the emission profile of the neutrons coming directly from the plasma. Fig. 5 shows such an emission profile as a function of the angle of incidence α which is defined in Fig. 2. For a collimator viewing only the central part of the plasma the ratio of the emitted and collided fluences would be essentially larger, but for such a measurement the neutron emission profile enters the determination of the total neutron yield and this introduces a new, large error.

Obviously, there is an optimal aperture angle for the collimator between the two extreme cases of observation of the full plasma diameter and the central part. This optimum has to be determined be VINIA calculations.

Results

Finally, we present in table 1 first results for absolute neutron yields determined by emulsions and VINIA calculations. For these measurements only the neutron spectrum between 2.1 and 3 MeV was used. The results agree very well with those from the counters. In view of the fact that the emulsion measurement, the VINIA calculation, and the calibration of the counters are completely independent, this good agreement confirmes our method of absolute yield determination with emulsion as well as the calibration of the counters.

Table 1

ASDEX discharge	P_{90^o} [proton tracks]	F [10^{-8} cm^{-2}]	$Y_{emulsion}$ [10^{13} neutrons]	$Y_{counter}$ [10^{13} neutrons]
16910	1485 ± 12%	2.52 ± 2.3%	1.2 ± 12.2%	1.3 ±15%
19111	2145 ± 12%	8.64 ± 6.5%	3.1 ± 13.6%	3.2 ±15%

References

[1] G. Assi, H. Rapp: A Neutron Flux Measurement System for ASDEX, IPP III/70, 1981

[2] K. Hübner, e.a., 14th Europ. Conf. on Controlled Fusion and Plasma Physics, Madrid 1987, part 3, pp 1298-1301, and Report IPP III/122, August 1987

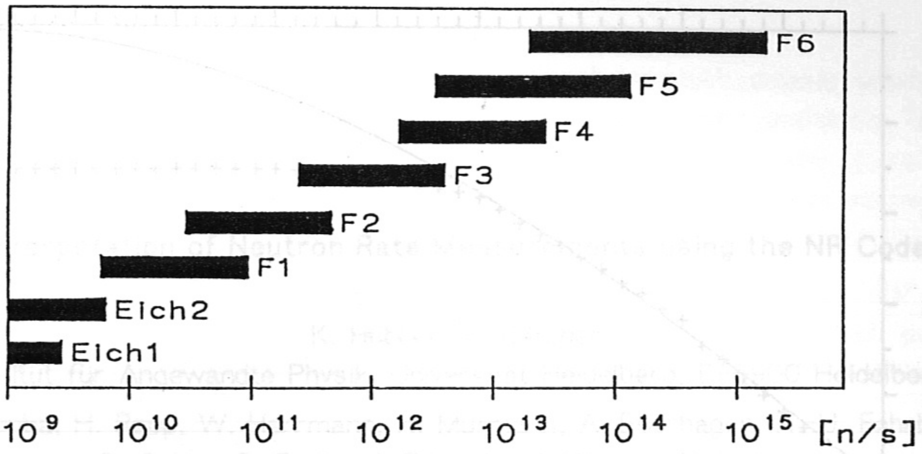

Fig. 1: Effective ranges of the neutron counters used at ASDEX

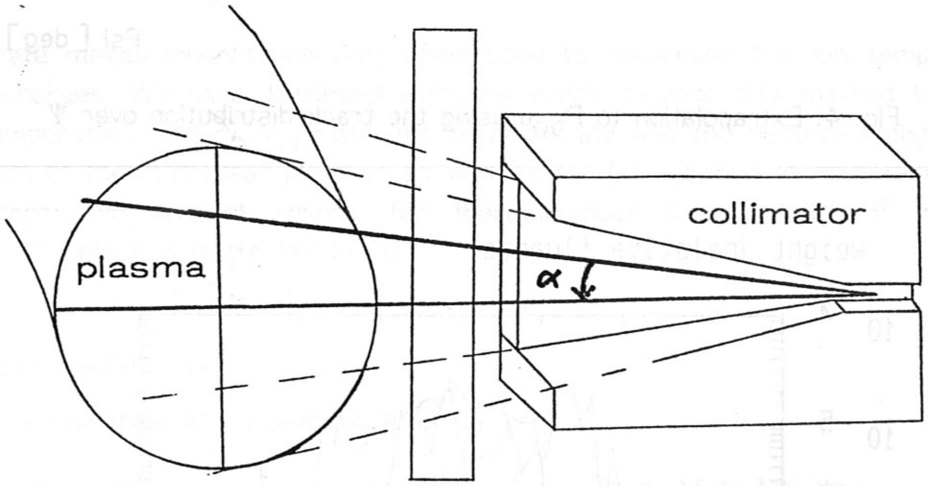

Fig. 2: Vertical cut through plasma and collimator, α is the vertical angle of incidence

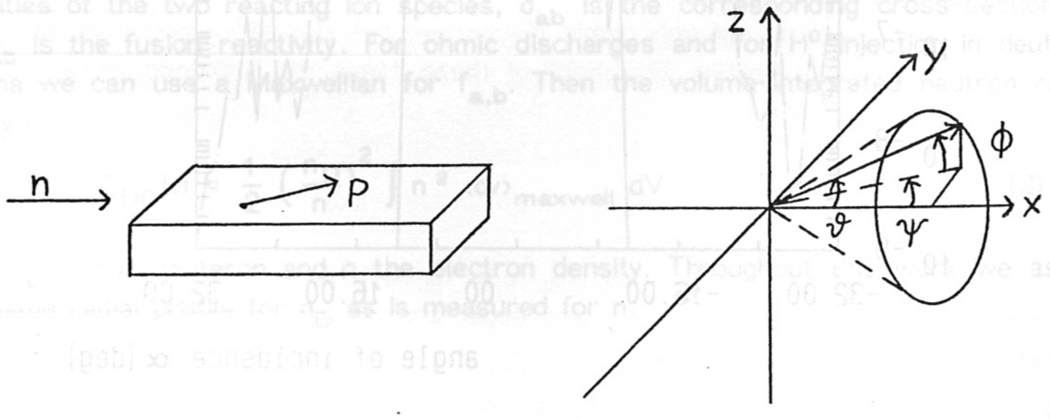

Fig. 3: Proton track angles in the emulsion

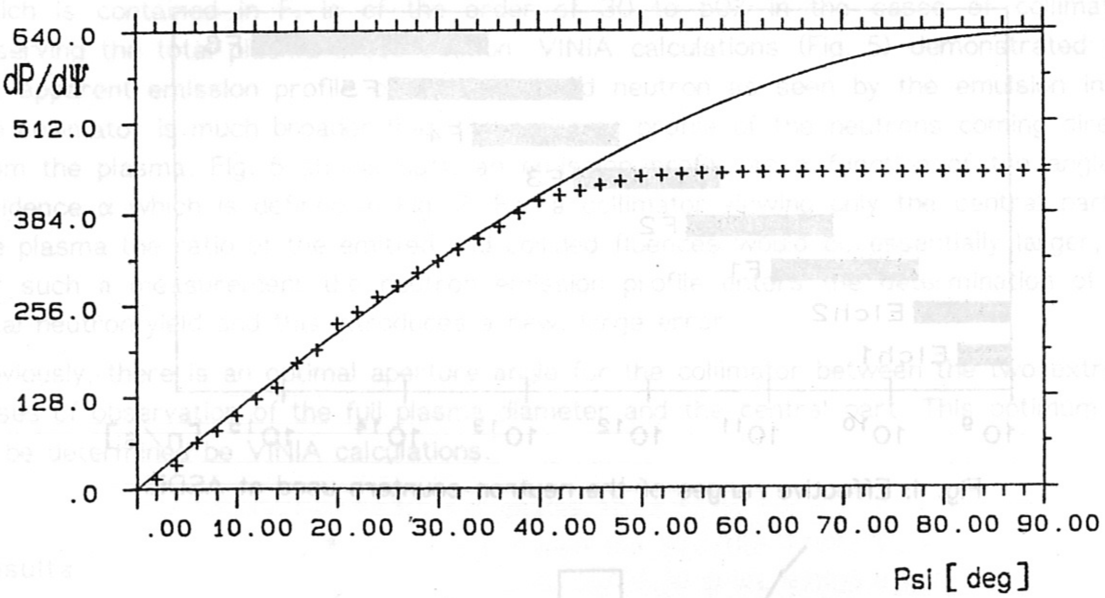

Fig. 4: Extrapolation to P_{90° using the track distribution over Ψ

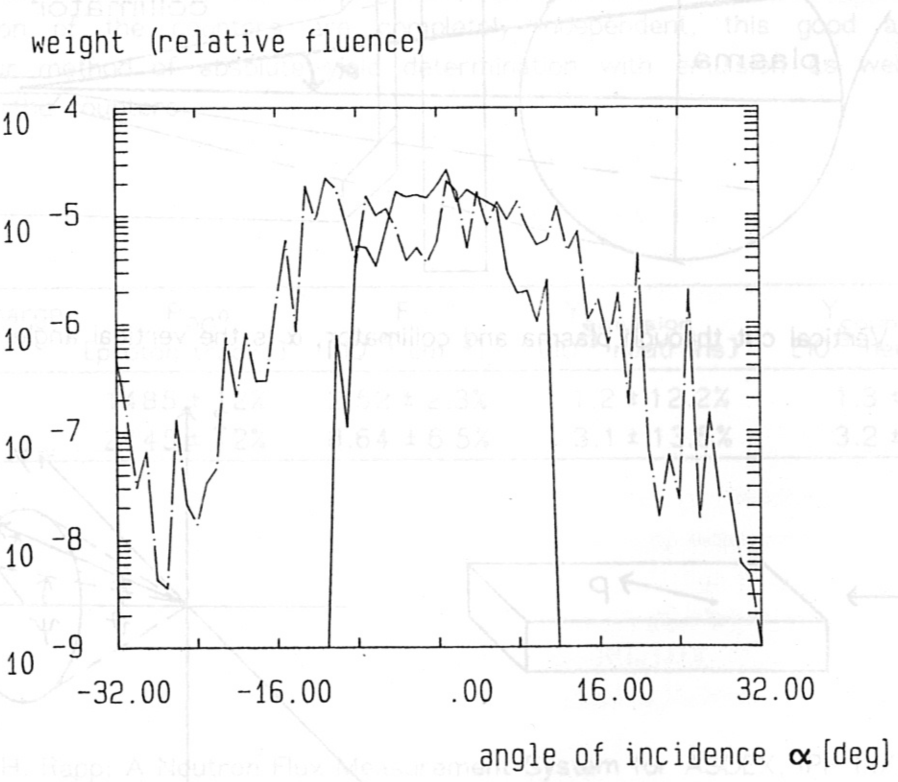

Fig. 5: Emitted (—) and collided (-·-) fluence at the emulsion as a function of α

Interpetation of Neutron Rate Measurements using the NR Code

K. Hübner, R. Bätzner
Institut für Angewandte Physik, Universität Heidelberg, D-6900 Heidelberg
B. Bomba, H. Rapp, W. Herrmann, H. Murmann, A. Eberhagen, H.-U. Fahrbach,
O. Gehre, R. Preis, H. Röhr, K.-H. Steuer, O. Vollmer
Max-Planck-Institut für Plasmaphysik, EURATOM Association, D-8046 Garching

Neutron rate measurements are very often used to determine the ion temperature in ohmic discharges. We have developed software which extends this method to calculate the ion temperature, the n_D/n_H ratio, the neutron rate and the neutron emission profile for all kinds of thermonuclear plasmas as well as for D^0 injection in deuterium plasmas. In this paper we present results for thermonuclear plasma with H^0 injection in deuterium; D^0 injection is treated in [1].

Theoretical model

The local neutron rate in a plasma is given by

$$Q_{a,b}(r,t) = n_a n_b \langle\sigma v\rangle_{ab} = n_a n_b \iint \sigma_{ab} |v_a - v_b| \, f_a(v_a) \, f_b(v_b) \, dv_a dv_b , \qquad (1)$$

where n_a, n_b, f_a, f_b, v_a, v_b are, respectively, the densities, distribution functions, and velocities of the two reacting ion species, σ_{ab} is the corresponding cross-section, and $\langle\sigma v\rangle_{ab}$ is the fusion reactivity. For ohmic discharges and for H^0 injection in deuterium plasma we can use a Maxwellian for $f_{a,b}$. Then the volume-integrated neutron rate is simply

$$Q_{DD}(t) = \frac{1}{2} \left(\frac{n_D}{n} \right)^2 \int n^2 \langle\sigma v\rangle_{maxwell} \, dV . \qquad (2)$$

Here n_D is the deuteron and n the electron density. Throughout this work we assume the same radial profile for n_D as is measured for n.

Interpretation of neutron rate

The volume-integrated neutron rate is completely determined by the geometric data of the plasma, the electron density and temperature profiles $n(r)$ and $T_e(r)$, the profile

$Z_{eff}(r)$, and the plasma deuteron density and temperature profiles $n_D(r)$ and $T_D(r)$. The densities of electrons, deuterons , and protons n_H are related by where Z_x is the

$$\frac{Z_x - Z_{eff}}{Z_x - 1} = \frac{n_D}{n}\left(1 + \frac{n_H}{n_D}\right), \tag{3}$$

charge of the dominant impurity. In a deuterium plasma without protons, n_D could therefore be determined from Z_{eff}, and thus the ion temperature T_D from the measured neutron rate Q_{DD}. If there is any information about the shape of the ion temperauture profile, the neutron emission profile $Q_{DD}(r)$ can also be deduced. For plasmas with a mixture of protons and deuterons, as with H^0 injection in D plasma, one of the two parameters T_D and n_D/n_H can always be calculated from the neutron rate if the other is known. Table 1 lists all the plasma parameters needed and the corresponding diagnostics used at ASDEX.

Structure of the NR software

To take care of all these possibilities, our software has a fully modular structure. The scheme is shown in Fig. 1; firstly, the DATA FILES software reads all input data. It is thus easy to adapt changes in the ASDEX data files or to introduce new data which become accessible with the development of new diagnostics. An example of the last is the new $Z_{eff}(r)$ measurement from visible bremsstrahlung which is now availiable at ASDEX. Secondly, the reactivities and the distribution functions are determined in INTERMEDIATE CALCULATIONS.In the FINAL CALCULATIONS one of the parameters Q_{DD}, T_D, and n_D can always be calculated, the other two being taken as ALTERNATE INPUTS. The software thus allows not only determination of the ion temperature or density, but also prediction of neutron rates and therefore detailed studies of the influence of relevant plasma parameters on the neutron rate. The flexibility of the software allows us to treat not only ohmic discharges but also H^o injection in deuterium plasmas and ICR and LH heating. For most of these cases the hydrogen content of the plasma is the main problem.

Results from the NR code

As examples for the application of the NR code we will discuss results for long-pulse H^0 injection and for ohmic discharges, and especially we will compare results for co- and counter-injection.

During earlier discharges with 400 ms H^o co-injection the neutron rate Q(t) seemed to be constant, but during long-pulse heating it decreases (Fig. 2a). We consider results for the ASDEX discharge #22631 (P_{inj} = 2.4 MW, W_{inj} = 45 keV, 1.0 - 2.5 s, I_p = 380 kA, B = 2.2 T, n = 4.2×10^{13}cm^{-3}). Assuming a ratio $T_D/T_e = 1.2$, as determined previously [2], we find that the decrease in Q(t) is caused by the dilution of the deuterium by the injected hydrogen, as demonstrated by the results for the n_D/n_H ratio (Fig. 2b). For this discharge during the injection phase this ratio becomes nearly constant about 300 ms after the start of NBI. Inspecting the neutron emission profile (Fig. 2c), one recognizes a decrease of the maximum and an increase of the width at half-maximum.

To demonstrate the different output facilities of our software, we used T_D/T_e = 1.2 and the results for n_D/n_H from discharge #22631 (Fig. 2b) as input for discharge #21485 (P_{inj} = 1.35 MW, W_{inj} = 45 keV, 0.9 - 2.5 s, I_p = 380 kA, B = 2.2 T, n = $4.0\times10^{13}cm^{-3}$) and calculated Q(t). The results are compared with the measured values in Fig. 3, the agreement being quite good. On the other hand, we again used the n_D/n_H results from Fig. 2b as input for discharge #21484 (P_{inj} = 1.0 MW, W_{inj} = 41 keV, 0.9 - 2.5 s, I_p = 380 kA, B = 2.2 T, n = $3.9\times10^{13}cm^{-3}$) and determined $T_D(t)$ from the measured Q(t). These results are shown in Fig. 4. The resulting ion temperature is about 10% higher than the measured electron temperature.

For the comparison of results for co- and counter-injection we use the ASDEX discharges #21479 (co-injection, P_{inj} = 1.35 MW, W_{inj} = 41 keV, 0.9 - 2.5 s, I_p = 380 kA, B = 2.2 T, n = 4.2x10 cm) and #21621 (counter-injection. P_{inj} = 1.0 MW, W_{inj} = 41 keV, 1.0 - 1.7 s, I_p = 420 kA, B = 2.2 T, n = $6.0\times10^{13}cm^{-3}$).

First of all we observe a difference in the behaviour of the n_D/n_H ratio during co- and counter injection (Fig. 5). In the co-case the sum of the deuterium and hydrogen density is constant, while the ratio decreases. In contrast to this the sum and the ratio increases during counter-injection. The reasons for this behaviour may be the different amounts of injected hydrogen and possibly improved confinement of deuterium during the counter-injection.

Of course it is also possible to determine the averaged deuterium density $\overline{n}_D$ during ohmic discharges. This is demonstrated for ASDEX discharge #22951 (I_p = 320 kA, B = 2.2 T, n = $3.6\times10^{13}cm^{-3}$). Fig. 6 shows the calculated mean deuteron density developement during the D_2 gas puff of this discharge compared with the measured mean electron density.

References

[1] K. Hübner, e.a., 15th Europ. Conf. on Controlled Fusion and Plasma Physics, Dubrovnik 1988, P 7 H 86

[2] K. Hübner, e.a., 14th Europ. Conf. on Controlled Fusion and Plasma Physics, Madrid 1987, part 3, pp 1294-1297

TABLE 1

Plasma data	Diagnostic
electron temperature	electron cyclotron emission or Nd:YAG Thomson scattering
electron density	HCN interferometry or Nd:YAG Thomson scattering
effective charge	bremsstrahlung
ion temperature	X-ray spectroscopy or CX spectroscopy or nuclear emulsion measurements
charge and density of impurities	visible spectroscopy
neutron rate	BF$_3$ and uranium counters
hydrogen and deuterium densities	CX spectroscopy

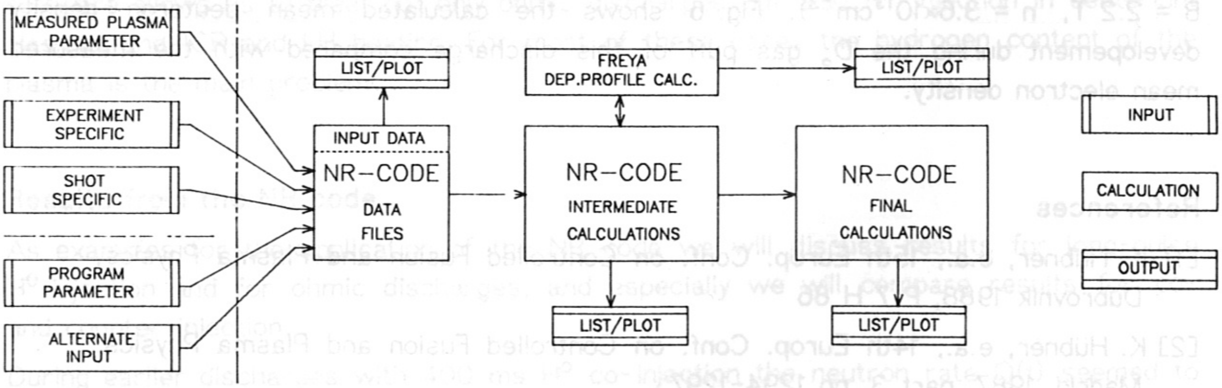

Fig. 1: Software scheme

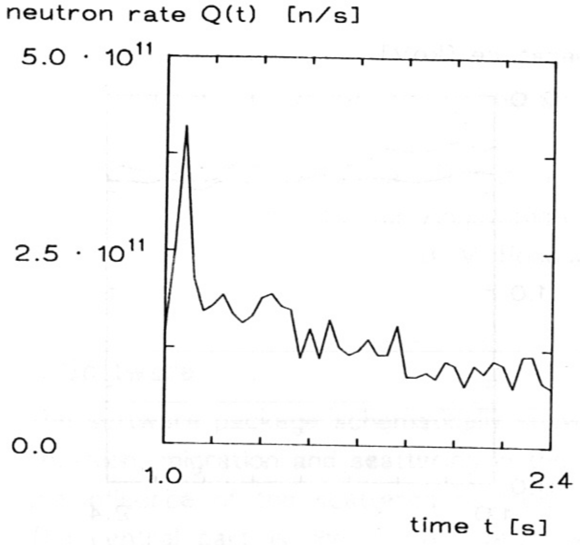

Fig. 2a: Measured neutron rate during long-pulse heating

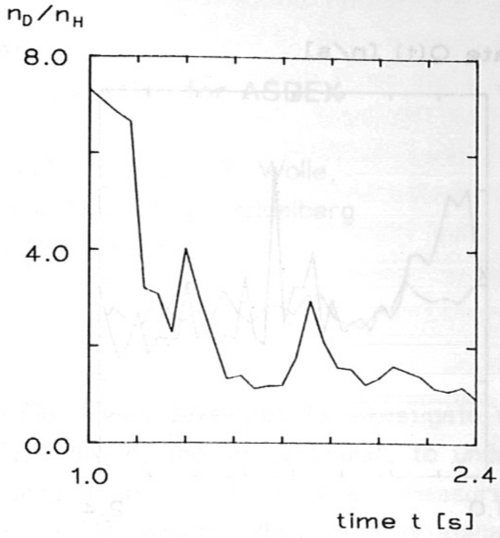

Fig. 2b: Calculated n_D/n_H ratio during long-pulse heating

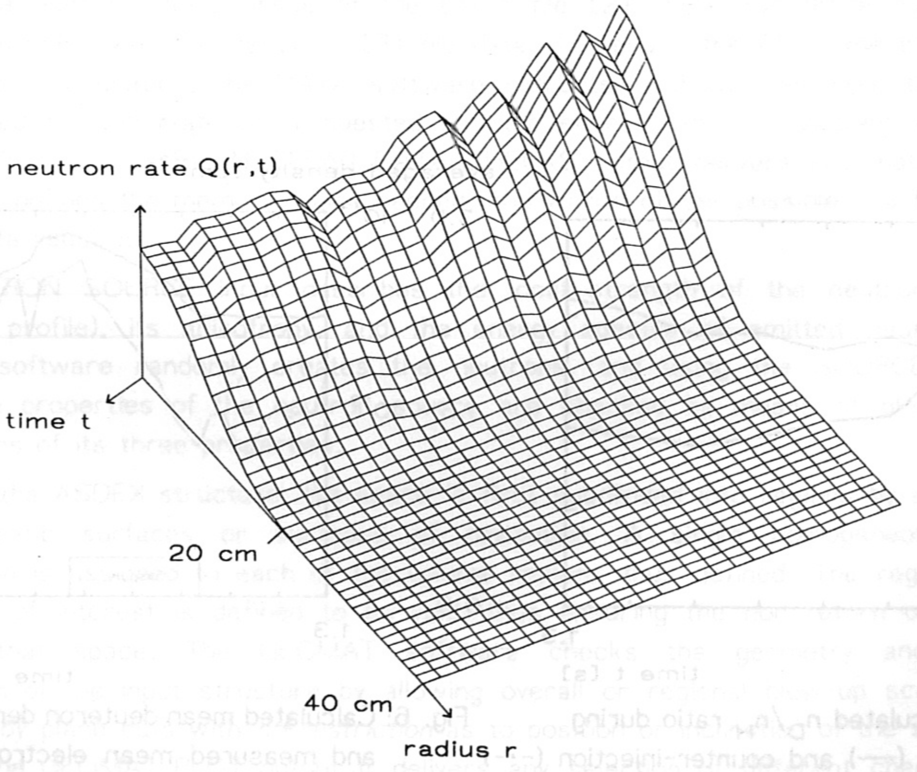

Fig. 2c: Calculated neutron emssion profile

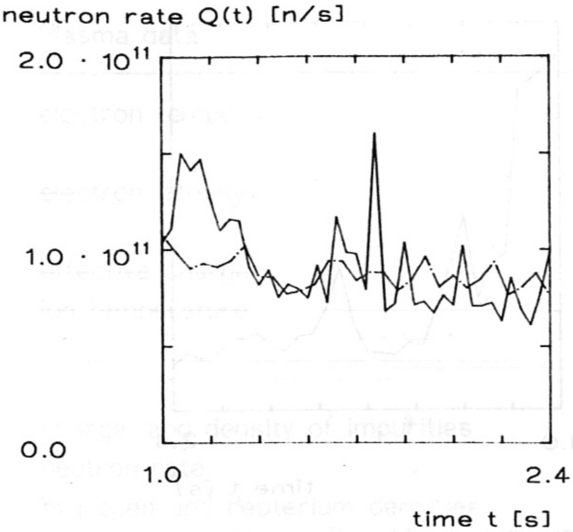

Fig. 3: Measured (—) and calculated (-··-) neutron rate

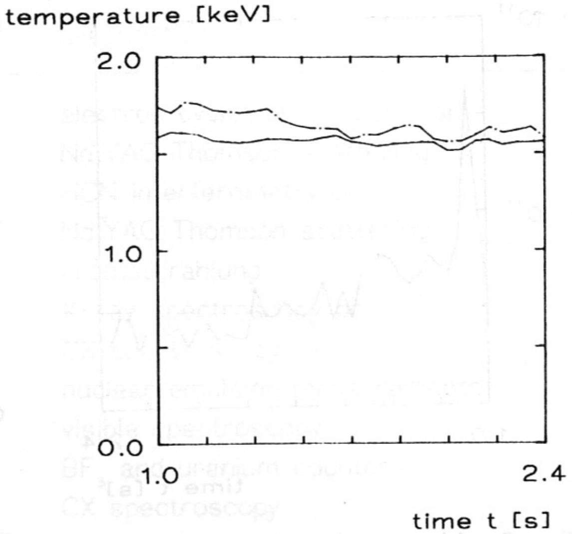

Fig. 4: Calculated deuteron temperature (-··-) and measured electron temperature (—)

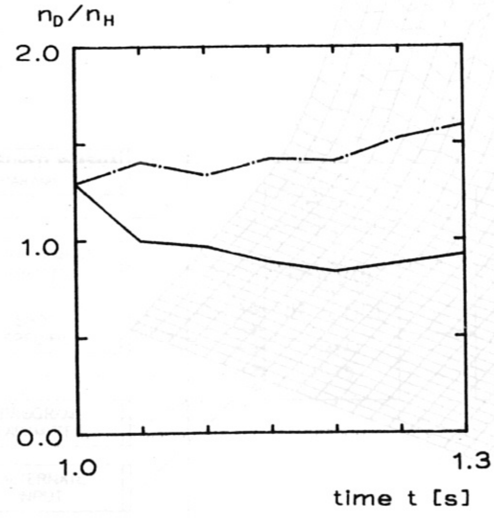

Fig. 5: Calculated n_D/n_H ratio during co- (—) and counter-injection (-··-)

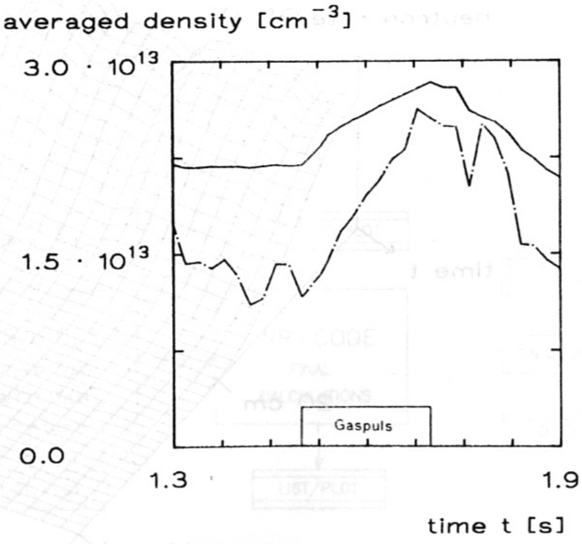

Fig. 6: Calculated mean deuteron density (-··-) and measured mean electron density during a deuterium gas puff

Calculation of Neutron Propagation for ASDEX

K. Hübner, R. Bätzner, R. Klein, M. Roos, B. Wolle,
Institut für Angewandte Physik, Universität Heidelberg
B. V. Robouch, ENEA, Frascati

1. Software

The software package schematically shown in Fig. 1 was developed to investigate neutron emission, migration and scattering in the ASDEX device, and, in particular, to understand the influence of the scattered neutron background on nuclear emulsion measurements. The central part is the VINIA-3DAMC software [1], which follows the propagation of each neutron through the ASDEX device and calculates for each neutron emission and collision the contributions to a desired detector (flux-at-a-point method). The program needs four inputs, namely nuclear data, neutron source, geometry and material distribution of the ASDEX structure.

The necessary nuclear data are available in standard nuclear data bank files (NDB FILES); we use the latest issue of the EFF 1 file [2], while for those nuclides not availiable in EFF 1 we take the JEF 1 [3] file data. To reduce the CPU time consumption and memory occupation, the DATA software extracts, without alteration, the nuclear data needed for the materials requested and the energy range considered and stores them in binary form. The NUCLEAR DATA CHECKS output delivers information on the data used, defines the memory space needed, and warns of the possible unavailiability of nuclide data required.

The NEUTRON SOURCE input describes the local strength of the neutron emission (emission profile), its anisotropy, and the energy spectra of emitted neutrons. The SOURCE software randomly creates the neutrons, and using the SOURCE CHECKS output the properties of the neutron source are checked by means of plots for the distributions of its three properties.

To define the ASDEX structure, the space is first subdivided into regions by using plane and quadratic surfaces or surfaces of revolution. A single homogeneous nuclide composition is assigned to each of the volume regions thus defined. The region beyond the space of interest is defined to be void, thus ensuring the non return of neutrons entering that space. The GEOMAT software checks the geometry and material distribution of the input structure by allowing overall or regional blow-up scans of the structure by plane cuts with *no restriction* as to position or inclination of the scan plane. Through the GEOMAT PLOT output it delivers any selection of different checks of the structure in respect of shape and material distribution.

While following the propagation of neutrons through the facillity, the VINIA-3DAMC software prepares the data of interest for the outputs. The GENERAL CHECKS output delivers information concerning the overall response of the structure to the emitted neutron fluence. The SPECTRAL FLUENCES output gives the neutron fluences and their spectral plots for a detector or a certain volume of interest whose extent is specified in the GEOMETRY input. These plots distinguish emission from collision as well as the three spatial zones possibly defined by a collimator, i.e. the open aperture and the semi-shadowed and shadowed zones. Furthermore, plots with and without the absorption of specified materials interposed between the detector and the contributing point of emission or collision are provided.

The ACTIVATION output stores all nuclides activated or generated by the neutrons considered, during their propagation through the facility. The T-BREEDING, BLANKET output serves for blanket studies [4] and is not used in the present work. Other physically significant outputs are available on request.

The DATA FILES FOR DETECTOR TREATMENT output stores, in the so-called PTO files, the neutron fluence contributions that are made by all events in all reaction channels to the detecting element considered, as well as the position of the event and the position of the detecting point. Using the PTO files, the NEPMC software [1] simulates the response function of the nuclear emulsion and stores the results in the NEP DATA FILES. Neutron and proton energy spectra as well as proton track distributions are plotted with the NEPLOT software from the NEP DATA FILES.

Monte Carlo software for simulating the response of He^3 spectrometers (HE3MC), spherical ionization chambers (IONMC), and activation samples (ACTMC) are under consideration.

2. ASDEX model

For our ASDEX model we distinguish six different groups of the geometric structure accordingly to their significance for the scattering of neutrons. The model is described in detail in a forthcoming IPP report [5].

Group 1 consists of the core (central screw and wooden core), the 16 toroidal field coils which intersect in the central region, the ohmic coils OH1 to OH8, and the vertical field coils V1 to V4 together with the central multipole correction coils MC1. The remaining coils are neglected, mainly because of their remoteness from the detectors and their small masses as compared with the vessel and the multipole coils. Furthermore, for most of the measurements they are located outside the aperture fields. For the same reasons the support structure is not included in the model either.

Group 2 is the vessel containing the vacuum chamber and its thermal insulation. The divertor forms group 3. It is geometrically somewhat simplified, yet ensures the right amount of materials near their real position. Figure 2 gives a cut through the ASDEX model in the centre plane of a toroidal field coil, showing the geometric structure of the groups 1 to 3. Figure 3 shows a horizontal cut through the centre of the tokamak.

Group 4 of the model describes the torus hall, its ground, walls, roof, and the air. Part of the operator room is considered to be a pseudo-detector in order to allow calculation of the average spectral neutron fluences within that space.

Group 5 consists of the necessary details of the ports. These are the port for the YAG light scattering system, near which most of our neutron diagnostics is at present located, and the port for the CX measurements, of which material parts are in the observation field of our radial collimator 2. Finally, the group 6 contains all the details of the nuclear emulsion equipment, i.e. their supports and collimators. So far we have considered the following measuring positions, which are also shown in Fig. 3:

position 1: radial collimator 1, in front of YAG port,
position 2: radial collimator 2, next to the CX port,
position 3: tangential collimator 3, next to the YAG port,
position 4: tangential collimator 4, next to the YAG port,
position 5: uncollimated emulsion in front of YAG port.

3. Numerical results

First test runs of the VINIA-3DAMC software with the new ASDEX model using 1500 emitted neutrons were done for measuring position 5 using the measured plasma data from ASDEX discharge no. 18949. This discharge belongs to a series of 10 shots with H-injection into a deuterium plasma for which we exposed a nuclear emulsion at position 5 in order to study the neutron emission profile. The main plasma parameters are:

plasma current	380 kA,	central electron density	5×10^{13} cm^{-3},
central electron temperature	2.4 keV,	central ion temperature	2.9 keV,
injection power	3.5 MW.		

Fig. 4 gives the VINIA calculations of the spectral neutron fluence arriving at position 5 from the full solid angle; part 4.a is the total fluence, 4.b the emitted part, and 4.c the collided contribution. The integral values (given in neutrons/cm^2 per emitted neutron) are compared in the following table with the results of earlier calculations for positions 1 and 2 without collimators:

	Position 5	Position 2	Position 1
total fluence	10.8×10^{-7}	6.2×10^{-7}	2.3×10^{-7}
emitted part	3.9×10^{-7}	2.0×10^{-7}	0.6×10^{-7}
collided part	6.9×10^{-7}	4.2×10^{-7}	1.7×10^{-7}
ratio of collided to emitted fluence	1.8	2.1	2.7

The decrease of the emitted neutron fluence from position 5 to 1 is simply caused by the increasing distance. It is noteworthy that the collided fluence in the energy range considered (1 to 3 MeV) also decreases with increasing distance, while the ratio of the collided to the emitted fluence increases. These effects have to be studied in more detail, being of importance in choosing the positions for neutron diagnostics.

An essential feature of the VINIA calculations is to provide information about the origins of the scattered neutron fluence. We found for the contribution of the different groups of components in ASDEX the following contributions (in neutrons/cm^2 per emitted neutron):

	collided fluence	fraction of collided fluence	fraction pf total fluence
core and coils	0.121×10^{-6}	18%	11%
vessel	0.120×10^{-6}	17%	11%
divertor	0.036×10^{-6}	5%	3%
hall	0.006×10^{-6}	1%	1%
port 1	0.393×10^{-6}	57%	36%
collimators 3, 4	0.012×10^{-6}	2%	1%

The strong contribution of port 1 was to be expected for position 5, but it may be reduced by an appropriate shielding.

4. NEPMC calculations and experimental results

The NEPMC software is used to simulate the response of the nuclear emulsion [1]. Fig. 5 gives the results of NEPMC calculations for the proton and neutron energy spectra, the VINIA results being used as input. The total fluence as well as the emitted and collided contributions are again shown. For an uncollimated nuclear emulsion measurement the neutron energy spectrum is determined by differentiating the proton energy spectrum. In these NEPMC calculations we took into account all proton tracks with a projected track length in the emulsion plane larger than 10 µm and all protons with energies above 1 MeV. For the proton energy spectrum created by the emitted part of the neutron fluence one would expect in principle a constant value below about 2.4 MeV. The decrease to lower energies is caused by the limitation in track length projection. The increase in the proton spectrum created by the collided neutron at about 1.8 MeV is caused by the collided low-energy contribution clearly seen in Fig. 4.c.

The NEPMC results are to be compared with the experimental results shown in Fig. 6. Unfortunately, in scanning the emulsion the lower limit for the protons track projection was increased in several steps from 10 to 40 µm in order to save scanning time, because at that time we were only interested in the longest tracks for the investigation of the neutron emission profile [6]. Only the high-energy wing of the proton energy spectrum thus has a physical meaning. Here the agreement between numerical and experimental spectra is good; for the measurements the determination of the absolute values is not possible.

The low-energy wing of the measured neutron energy spectrum is remarkably broader than the numerical spectrum. This is mainly caused by the fact that the track length was determined simply from the starting and end points of the track, so that the measured length is systematically reduced owing to the bending of the tracks. This effect is so far not included in the NEPMC software; it causes shift and broadening of the low-energy wing of the neutron spectrum.

References

[1] K. Hübner, e.a., 14th Europ. Conf. on Controlled Fusion and Plasma Physics, Madrid 1987, part 3, pp 1298-1301, and Report IPP III/122, August 1987
[2] H. Gruppelaar, D. Nierop, EFF 1, Summary, Information, ed. ECN Physics Department Petten, Holland, 1986
[3] Nuclear Data Library, OCDE NEA Data Bank, Gif s'Evette, 1985
[4] J. S. Brzosko, e.a., IEEE Transactions in Plasma Science, PS-15, (1987), 16-27
[5] B. V. Robouch, e.a. Report IPP III/132, in preparation
[6] K. Hübner, e.a., 14th Europ. Conf. on Controlled Fusion and Plasma Physics, Madrid 1987, part 3, pp 1294-1297

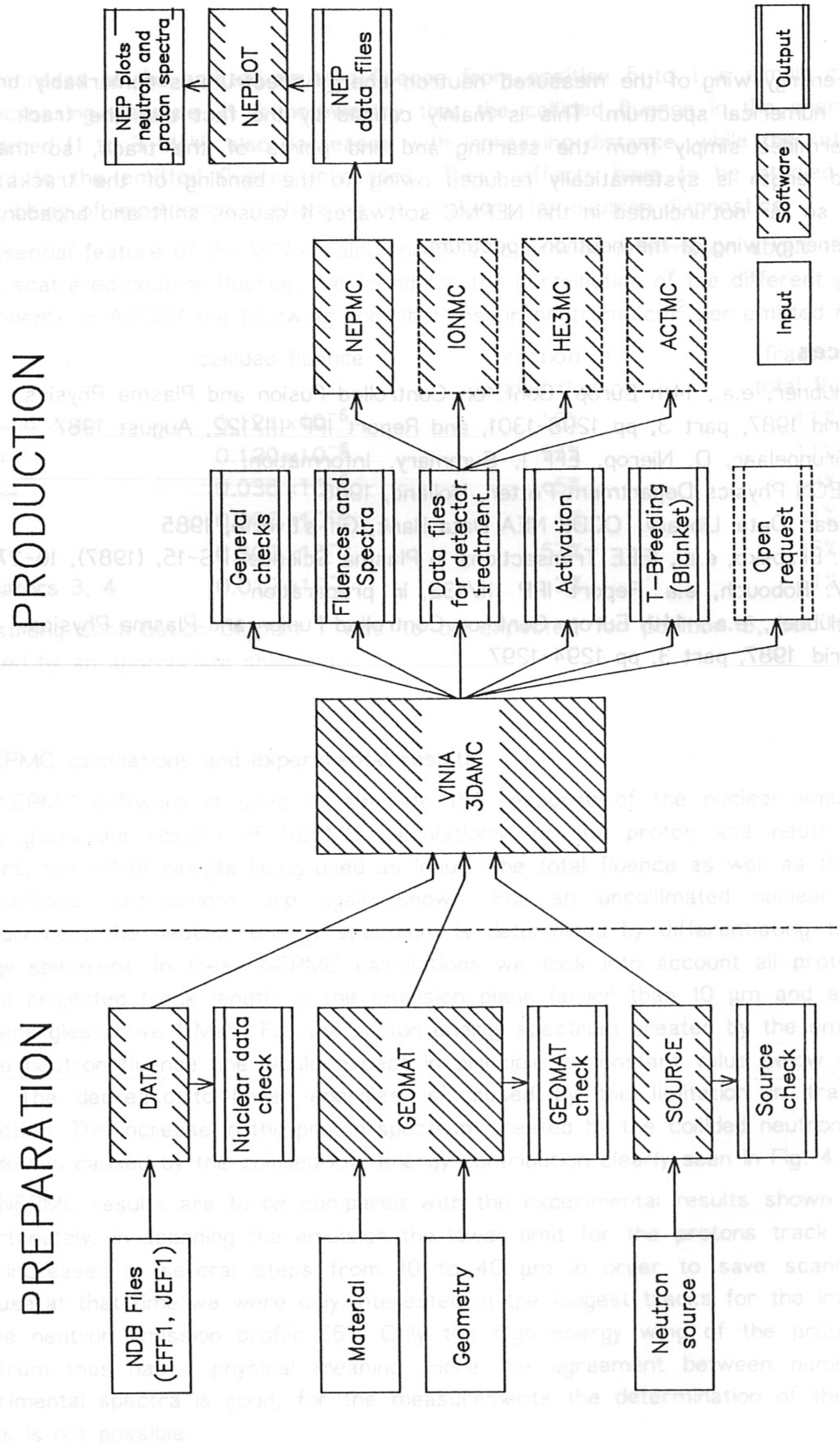

Fig. 1: Scheme of software package

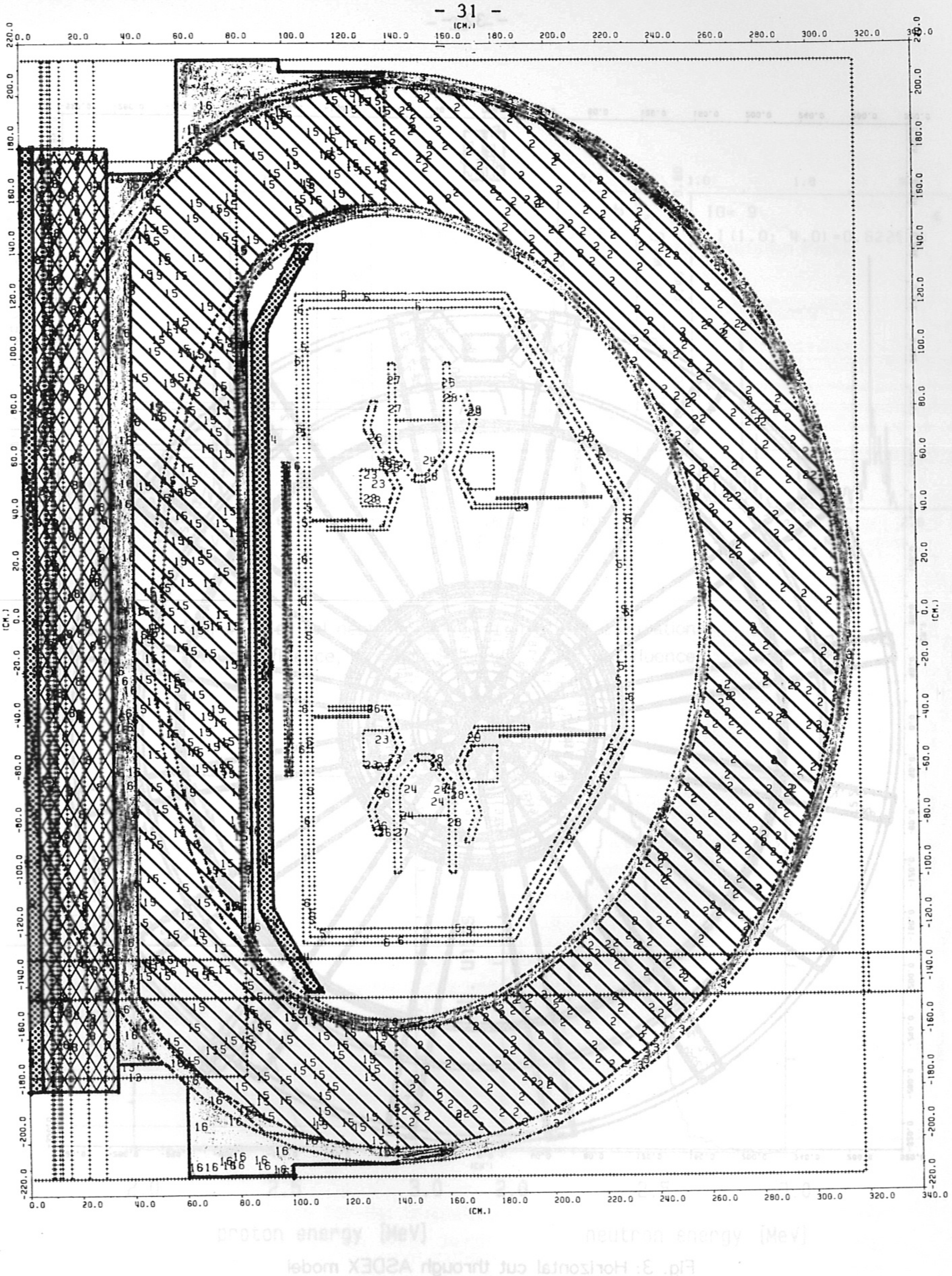

Fig. 2: Vertical cut through ASDEX model

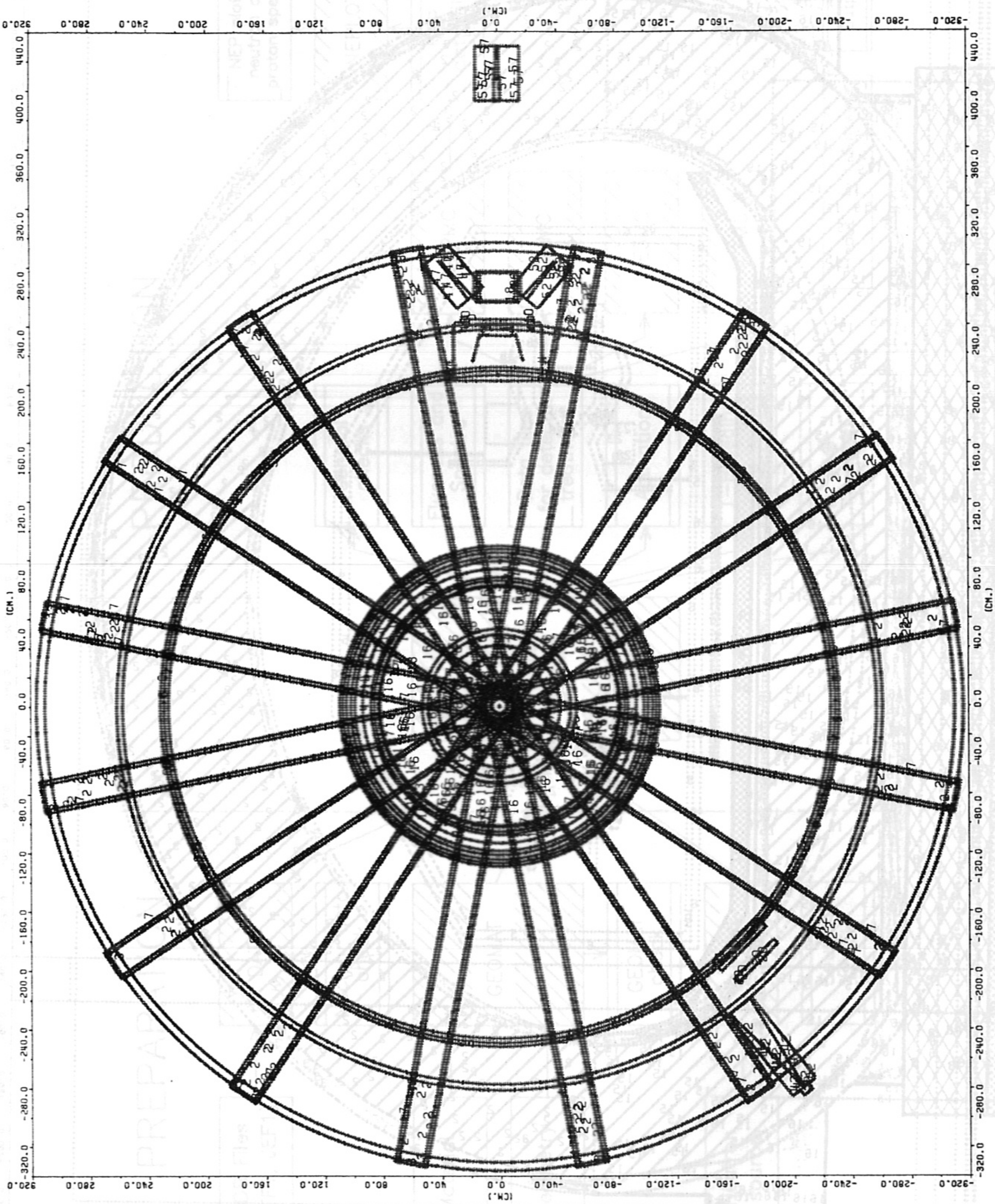

Fig. 3: Horizontal cut through ASDEX model

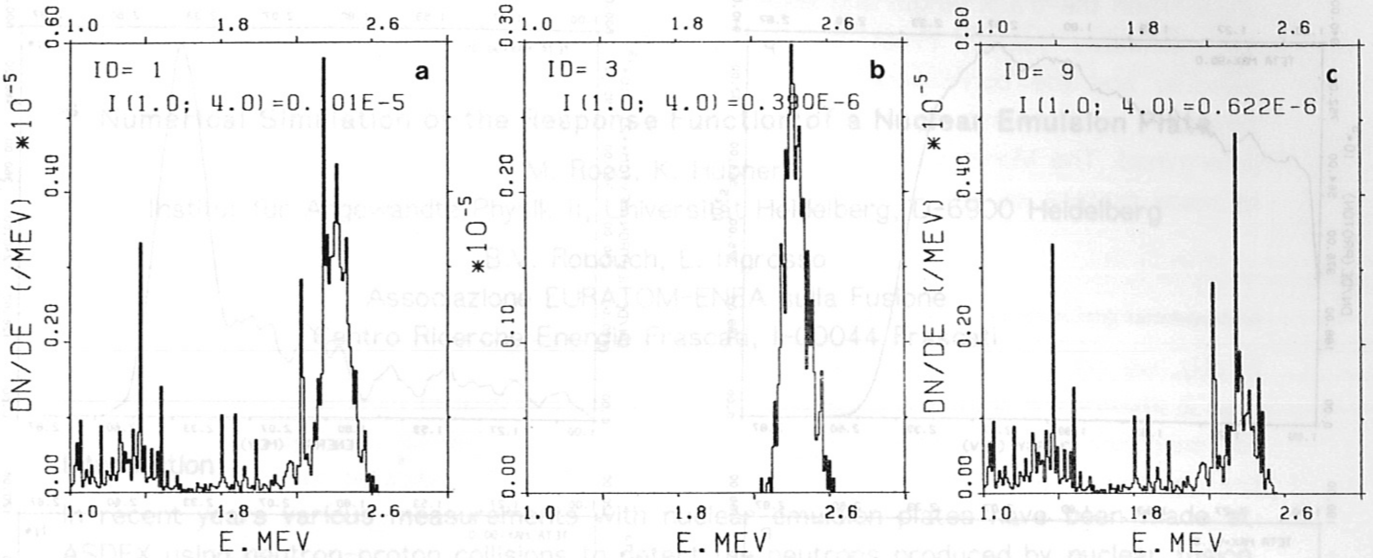

Fig. 4: Spectral neutron fluence from VINIA calculations
a: total fluence, b: emitted fluence, c: collided fluence

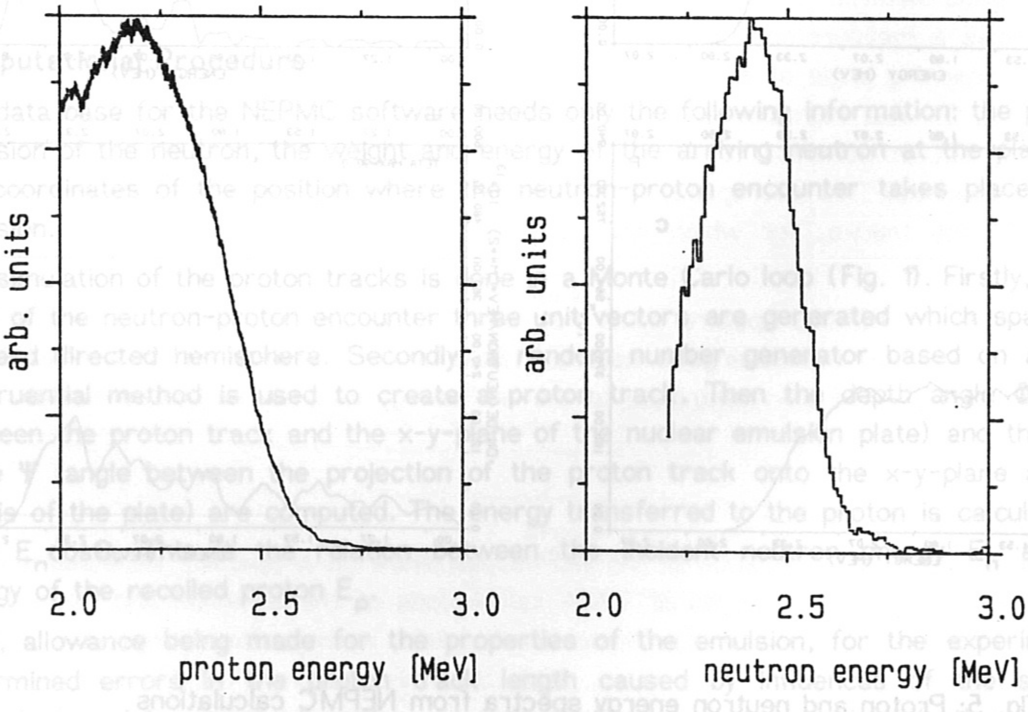

Fig. 6: Measured proton and neutron energy spectra

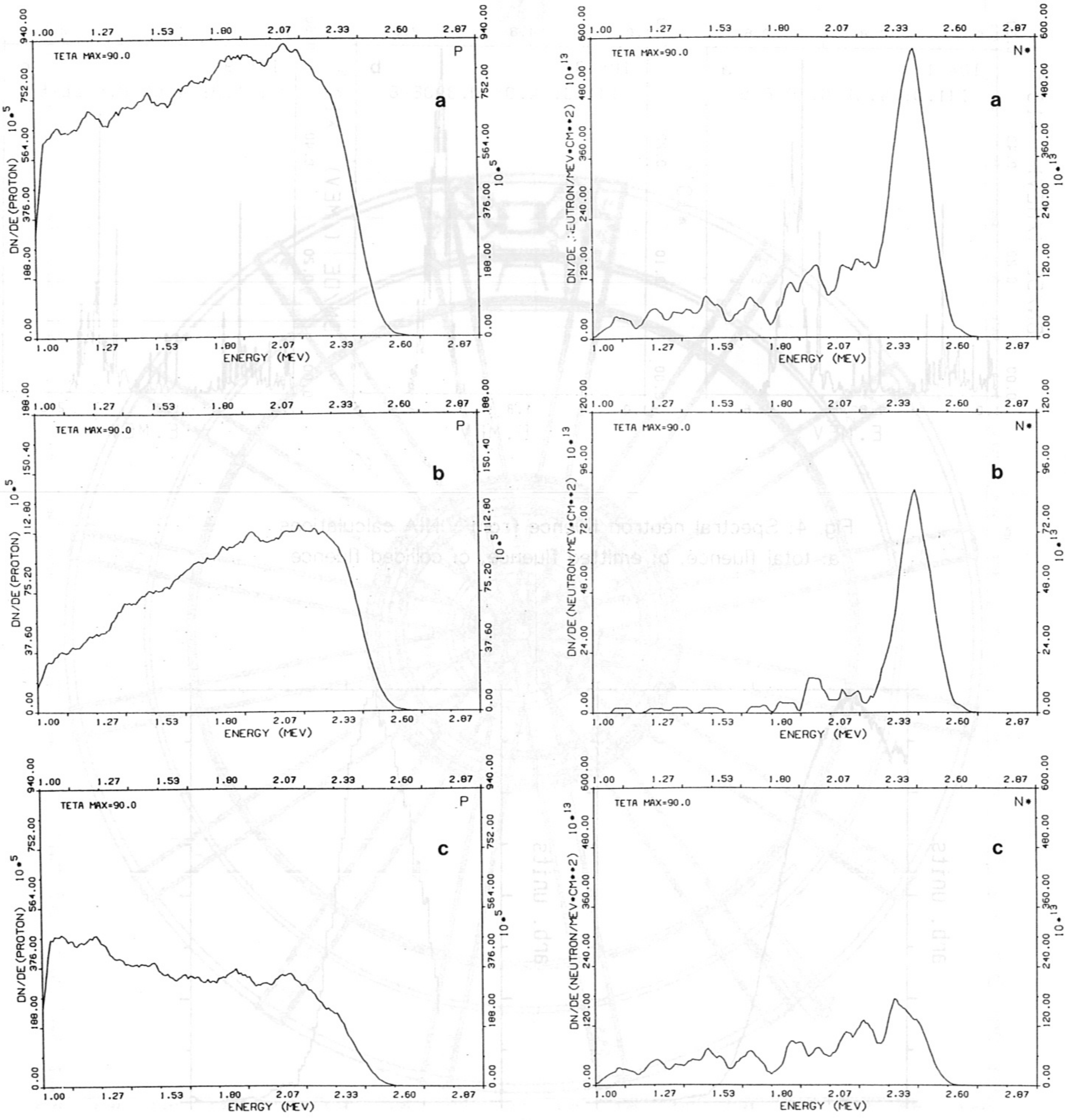

Fig. 5: Proton and neutron energy spectra from NEPMC calculations
a: total fluence, b: emitted fluence, c: collided fluence

Numerical Simulation of the Response Function of a Nuclear Emulsion Plate

M. Roos, K. Hübner
Institut für Angewandte Physik II, Universität Heidelberg, D-6900 Heidelberg

B.V. Robouch, L. Ingrosso
Associazione EURATOM-ENEA sulla Fusione
Centro Ricerche Energie Frascati, I-00044 Frascati

Introduction

In recent years various measurements with nuclear emulsion plates have been made at ASDEX using neutron-proton collisions to detect the neutrons produced by nuclear fusion processes. Along their way through the emulsion recoiled protons ionize silver bromide crystals. After development of the emulsion the tracks are searched and measured.

The Nuclear Emulsion Plate Monte Carlo (NEPMC) program was designed to simulate these proton tracks by using Monte Carlo algorithms and to determine the response function of the emulsion, i.e. the measured neutron spectrum for a given spectral neutron fluence arriving at the emulsion.

Computational Procedure

The data base for the NEPMC software needs only the following information: the point of emission of the neutron, the weight and energy of the arriving neutron at the plate, and the coordinates of the position where the neutron-proton encounter takes place in the emulsion.

The simulation of the proton tracks is done in a Monte Carlo loop (Fig. 1). Firstly, at the point of the neutron-proton encounter three unit vectors are generated which span up a forward directed hemisphere. Secondly, a random number generator based on a linear congruential method is used to create a proton track. Then the depth angle Φ (angle between the proton track and the x-y-plane of the nuclear emulsion plate) and the plane angle Ψ (angle between the projection of the proton track onto the x-y-plane and the x-axis of the plate) are computed. The energy transferred to the proton is calculated by $E_p = E_n \cos\Theta$. This is the relation between the incident neutron energy E_n and the energy of the recoiled proton E_p.

Next, allowance being made for the properties of the emulsion, for the experimentally determined errors in the proton track length caused by influences of the scanning procedure and by range straggling, as well as for the errors in the depth and plane angle. Then the track length and angles are perturbed with gaussian distributions around the calculated values. From these Gaussians a new proton track is stochastically selected and the corresponding neutron energy is calculated. With these results the simulated proton and neutron spectra are filled and thus the response function is determined. The Monte Carlo loop is done several times, so that it is possible to create as many protons as are desired out of one neutron input.

Monoenergetic point source

Firstly, we consider the response of a nuclear emulsion to a monoenergetic point source. Fig. 2 shows the proton and neutron energy spectra produced by the NEPMC program for maximum scanning angles $\Theta_{max} = 90^0$ and 30^0. Furthermore, off-axis incidence of the neutron of $\alpha = 10^0$ is assumed. The ideal response is indicated in Fig. 2 by dotted lines. The spectra show statistical fluctuations, the high-energy wing of the proton spectrum is smeared and the neutron spectrum is essentially broadened. This is caused by the errors mentioned and the off-axis incidence of neutrons, which together determine the response function.

The influence of the off-axis incidence is further demonstrated in Fig. 3. Here we used $\Theta_{max} = 30^0$ and $\alpha = 0^0, 10^0, 30^0$. Increasing α causes broadening and shifting of the spectra to lower energies. For $\alpha = 0^0$ the response is only determined by the errors in the measurement and the emulsion properties.

Monoenergetic neutron point sources are realized with accelerators. As an example Fig. 4 shows a measurement at the Gothenburg accelerator /1/. Here, too, we used a maximum scanning angle of 10^0. These measurements are to be compared with the last row in Fig. 3. The high-energy wing of the peak corresponds very well with our simulation. But in contrast to the simulated neutron spectra the low-energy wing is slightly broadened. This decrepancy is still under investigation. It may be caused by the bending of the tracks, for which we have up to now no simulation in the NEPMC program.

Furthermore, the NEPMC spectra could not contain the collided flux in the low-energy range, because only monoenergetic neutrons from a point source were used as input. This collided flux could also contribute to the low-energy wing of the measurement.

Extended neutron source

Next we consider the application of the NEPMC software on a spatially extended source. Here as input we use the results of VINIA calculations of the emission and migration of neutrons in the ASDEX device [1]. These results yield, among other things, the position and material for each neutron collision. With this information the NEPMC program is capable of simulating the neutron spectra of all arriving neutrons or of separately considering the contributions from certain materials to the spectra. Fig. 5 shows an example of simulated spectra for different scattering materials. It can observed that the quartz window is one of the major sources of collided neutrons. Detailed results of NEPMC calculations for ASDEX are discussed in [1] and [2].

References

[1] K. Hübner, e.a., 14th Europ. Conf. on Controlled Fusion and Plasma Physics, Madrid 1987, part 3, pp 1298-1301, and Report IPP III/122, August 1987

[1] K. Hübner, e.a., 15th Europ. Conf. on Controlled Fusion and Plasma Physics, Dubrovnik 1988, P 3 A1 03

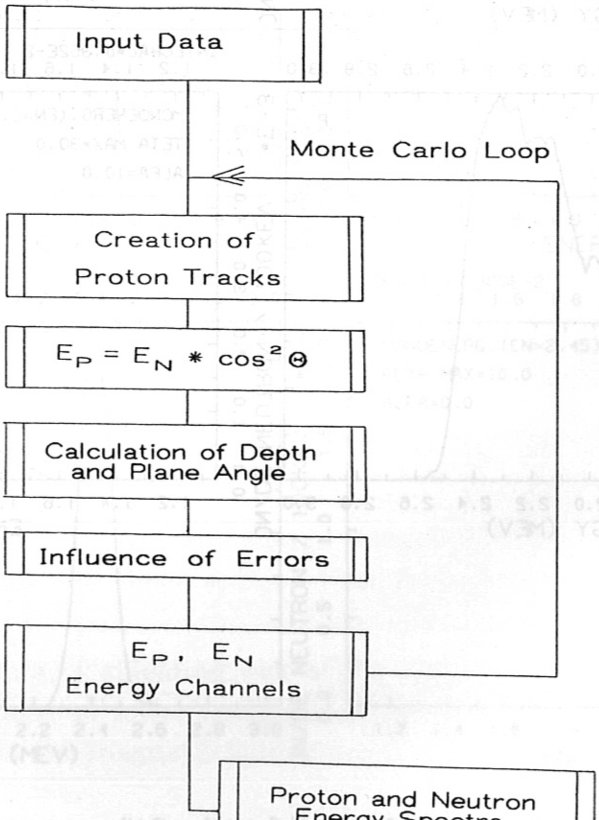

Fig. 1: Software scheme

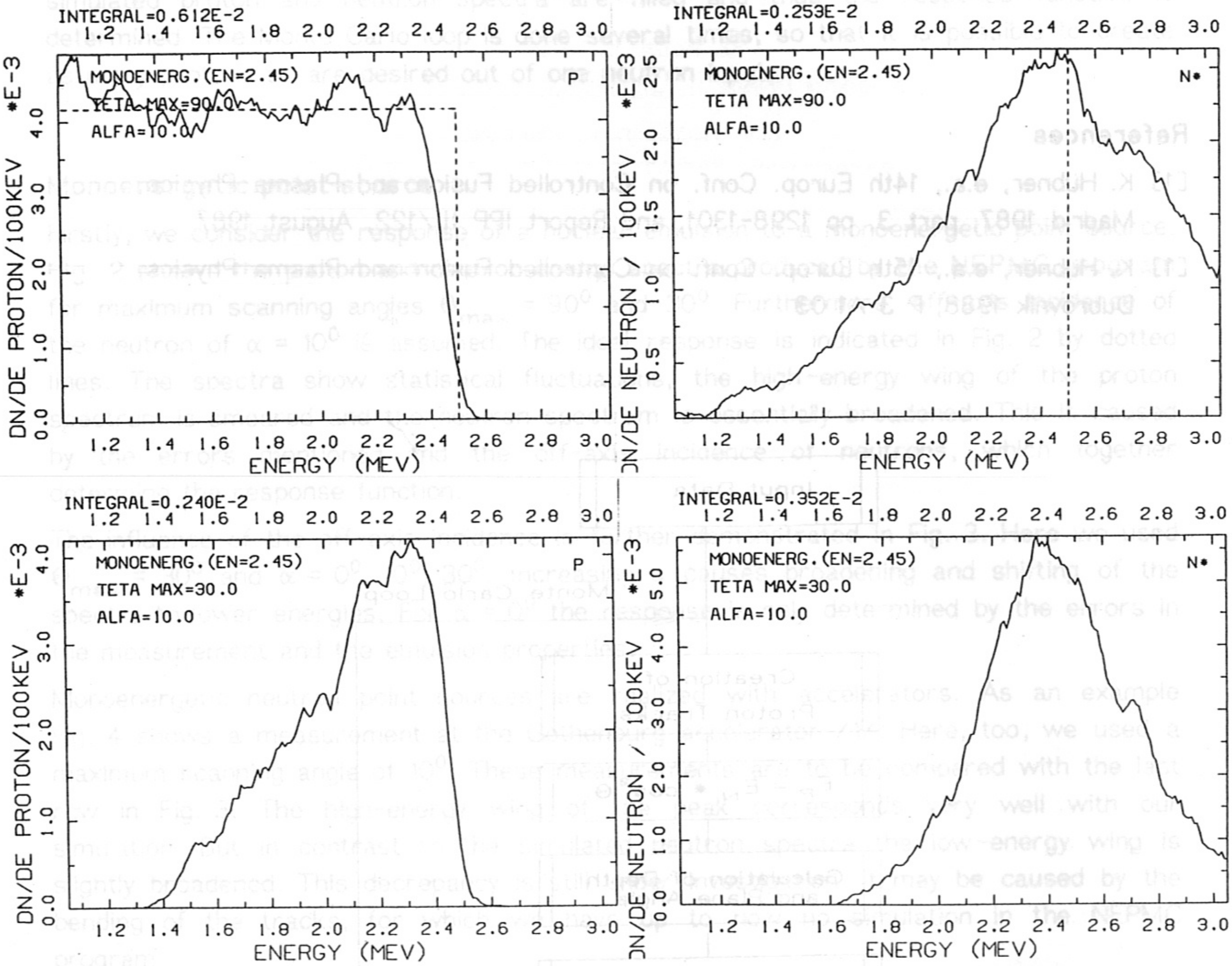

Fig. 2: Simulated proton spectra (left column) and neutron spectra (right column) for maximum scanning angles of $\Theta_{max} = 90^0$ (a) and $\Theta_{max} = 30^0$ for a constant angle of incidence $\alpha = 10^0$. The dotted lines shows the ideal response for a monoenergetic point source.

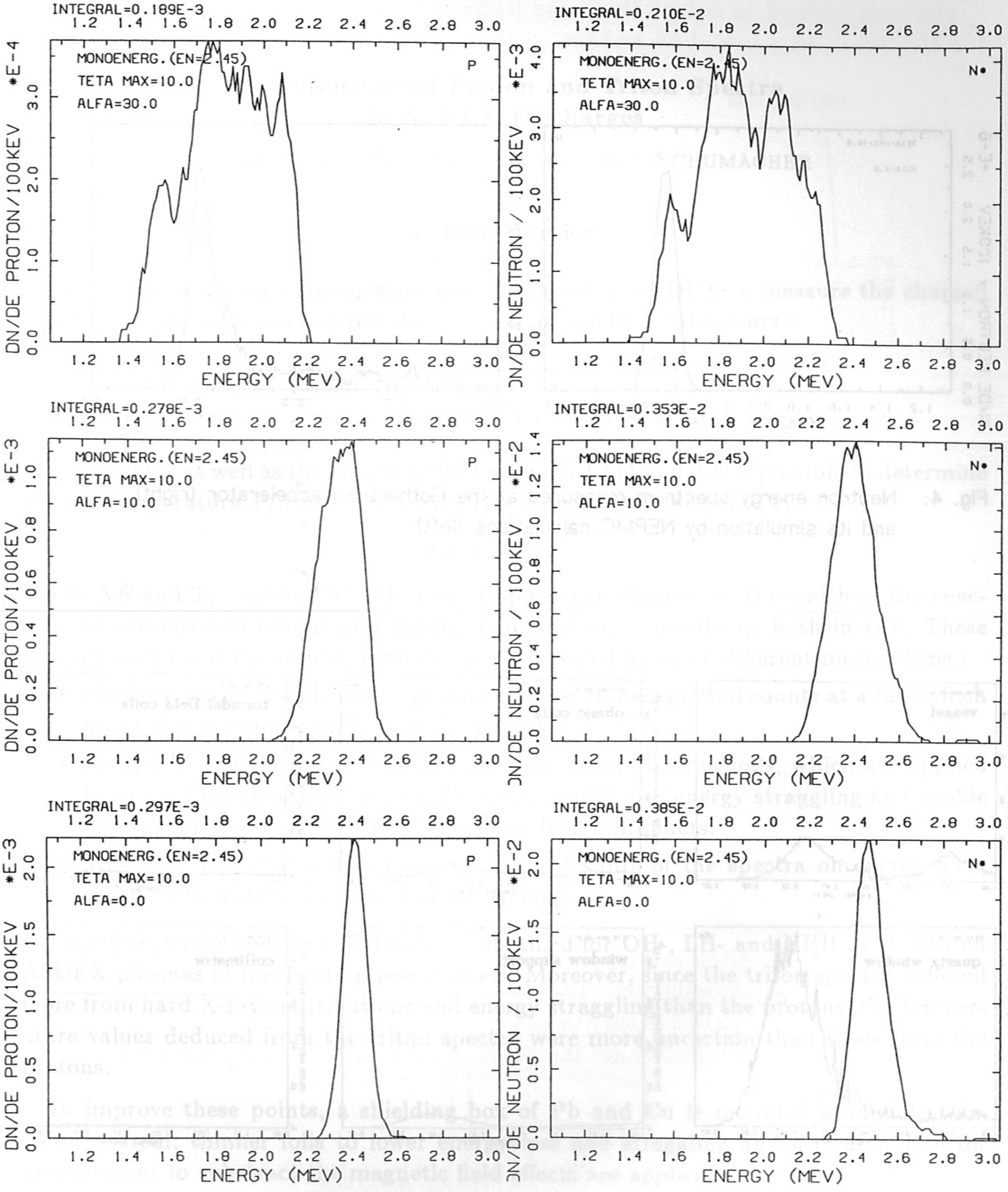

Fig. 3: Simulated proton spectra (left column) and neutron spectra (right column) for a maximum scanning angle of $\Theta_{max} = 10^0$ and different angles of incidence $\alpha = 30^0, 10^0, 0^0$.

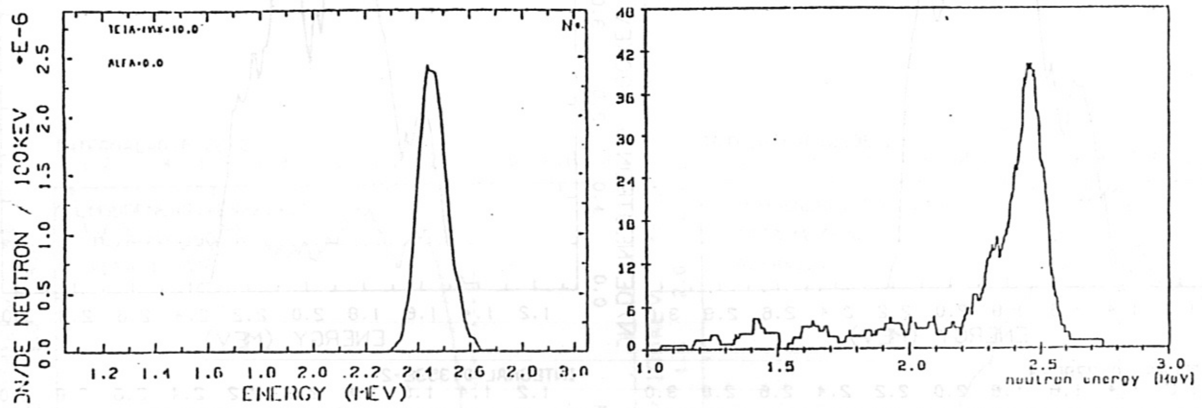

Fig. 4: Neutron energy spectrum measured at the Gothenburg accelerator (right) and its simulation by NEPMC calculations (left)

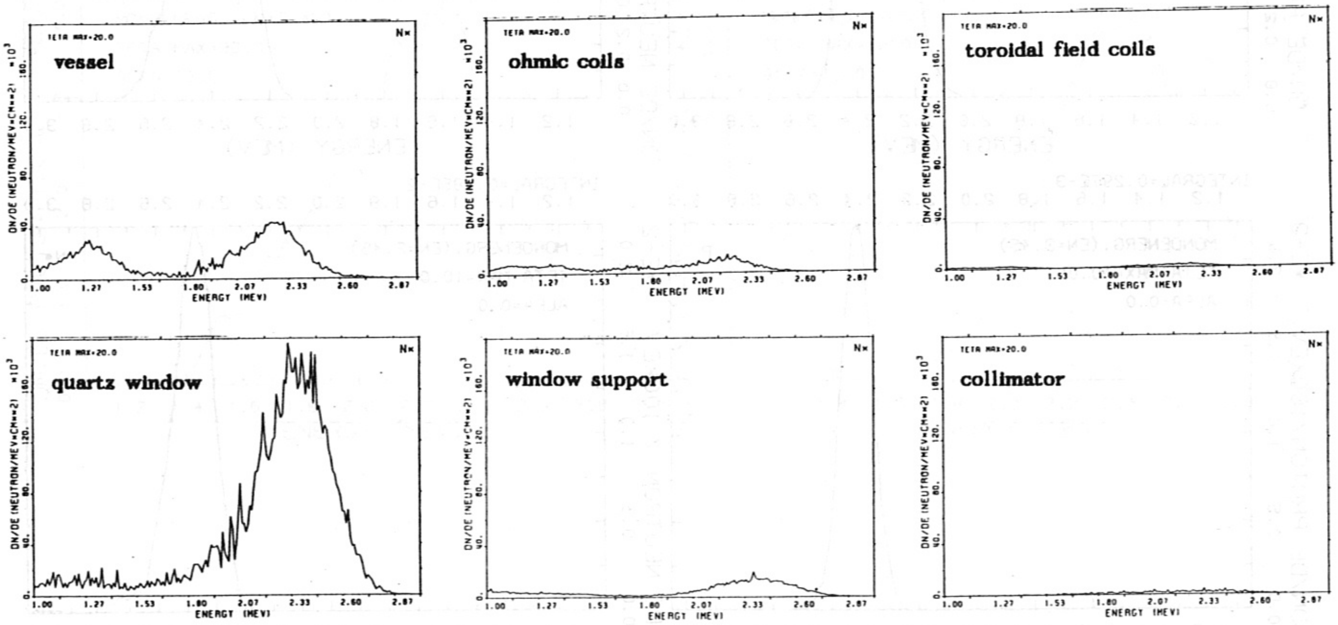

Fig. 5: Simulated neutron spectra for different scattering materials in the ASDEX facility (identical scales)

Measurements of Proton and Triton Spectra in ASDEX Discharges

E.SIMMET,U.STROTH,H.-S.BOSCH,U.SCHUMACHER

1. Introduction

Recently a new diagnostic method was developed on ASDEX to measure the charged fusion products from the d-d-reactions with semi-conductor detectors :

$$d + d \rightarrow p(3.02MeV) + t(1.01MeV)$$

$$d + d \rightarrow n(2.45MeV) +^3 He(0.82MeV)$$

The protons as well as the tritons could be detected {1} and it was possible to determine the ion-temperature T_i from both of the species using the formula {2}

$$\Delta E = 91.6\sqrt{T_i}$$

where ΔE and T_i are the FWHM of the Doppler contribution to the width of the spectrum of protons and tritons and the ion-temperature, respectively, both in keV. These measurements and the results, however, are influenced by three different mechanisms :

- Hard X-rays emitted from the plasma give rise to background counts at a rate which drops about exponentially with the energy.
- Energy loss of the charged fusion products occurs in thin foils, which are applied to protect the detector from visible light, resulting in energy straggling and profile broadening, especially for too low energy fusion products.
- Magnetic field changes lead to uncontrolled shifts of the spectra on energy axis, resulting in a statistical spectral broadening.

Therefore, so far spectra could only be obtained for OH-, LH- and NI(H in D)-heated ASDEX plasmas at low heating power levels. Moreover, since the triton spectra suffered more from hard X-ray contributions and energy straggling than the protons, the temperature values deduced from the triton spectra were more uncertain than those from the protons.

To improve these points, a shielding box of Pb and Cu is mounted around the detector system, thinner foils to lower energy loss and straggling and a double detector arrangement to substract the magnetic field effects are applied.

2. The Detection System

Fixed at a manipulator (see Fig.1), two semi-conductors with an energy resolution of about 10 keV and a dead layer of 200 nm mounted in parallel can be moved close to the plasma edge. Since the magnetic influences are identical in these two circles they can be eliminated by forming the difference of the signals.

The best method to reduce the X-ray background is to shield the detectors in their plastic capsule by a box of Pb and Cu, as shown in Fig.2.

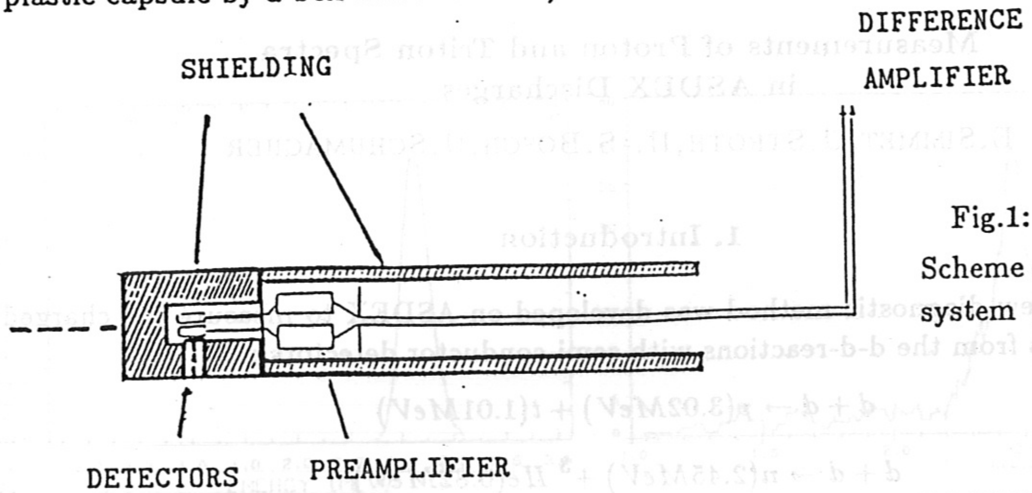

Fig.1:
Scheme of the detection system

Fig.2:
Parts of the detector head:
Detector,collimator,plastic capsule and shielding

Due to the large energy loss of the tritons in the recently used 5 μm thick Al foils, the triton spectrum often overlapped with the low energy background, such that this spectrum could not be evaluated. The use of a new plastic foil (Hostaphan,$C_{10}H_8O_4$) will raise the resulting triton energy to about 850 keV compared to 500 keV before. This is an important improvement to get the peaks out of the X-ray background and to avoid a large fraction of energy straggling.

3. Fast Ion Orbits in ASDEX

In order to be able to unfold the measured spectra, trajectory calculations have to be performed {3}. These calculations are also necessary to find the appropriate position and direction of the collimator. In Fig.3 trajectories for protons and ^3He are shown for the same collimator coordinates and the same set of plasma parameters.

Because of momentum conservation in the fusion reaction the protons and the tritons, with identical charges, have the same orbits.

The ^3He-ions reaching our system, however, come from different regions of the plasma and, therefore, have other probability- profiles than the protons or tritons.

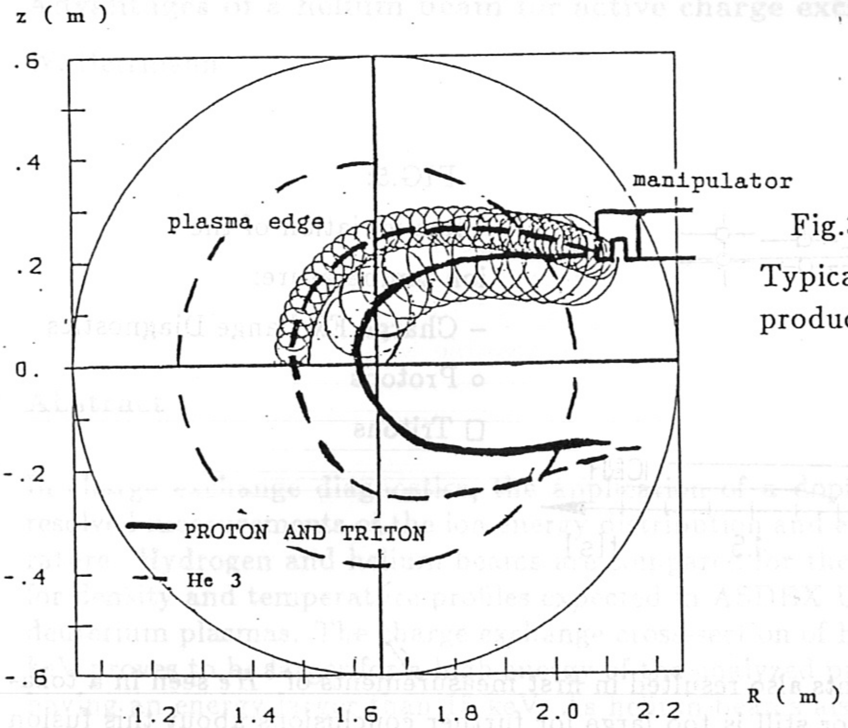

Fig.3:

Typical trajectories of the fusion products in ASDEX

4. Proton and Triton Spectra

In Fig.4. we show a spectrum which has been measured during an ICRH-heated phase of an ASDEX discharge. Here the triton peak is well separated from the X-ray background. This background, which in former times often extended up to the energy of 1 MeV, now is reduced by more than 50%. Also the test pulse spectrum showing the electric and magnetic influence is rather small and does not drift away.

For this shot an ion-temperature of 1.8 keV was deduced from the proton spectrum as well as from the triton spectrum.

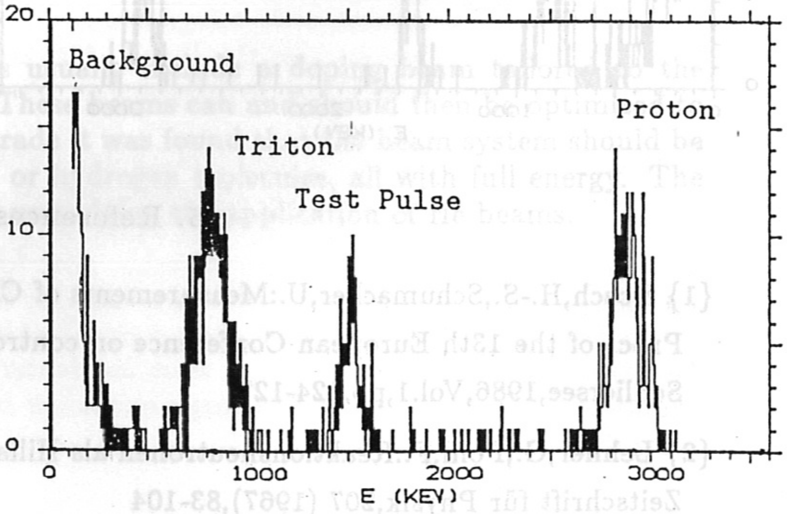

Fig.4:
Charged fusion products during
an ICRH-NI-discharge of ASDEX
(# 22653)

In Fig.5 the time variation of the ion-temperature during an NI-heated discharge as measured from the protons and the tritons is compared with the results of the charge-exchange diagnostics.

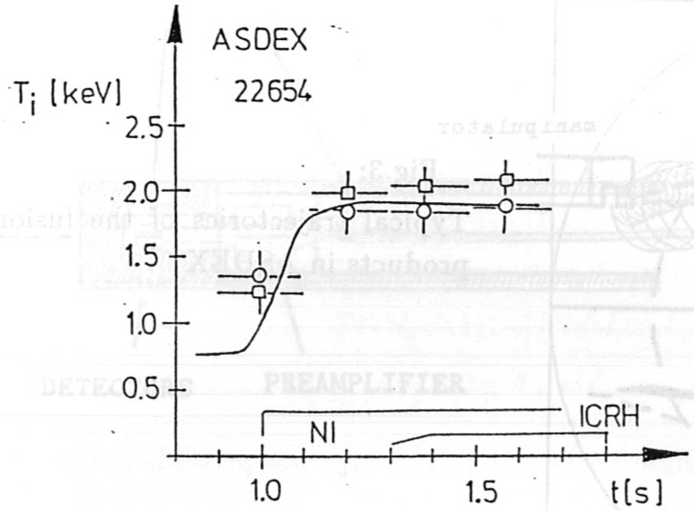

FIG.5:

Time variation of the ion-temperature:

– Charge Exchange Diagnostics

○ Protons

☐ Tritons

The described improvements also resulted in first measurements of ^3He seen in a tokamak. But the statistical error still is too large for further conclusions about this fusion product. Such a spectrum is shown in Fig.6.

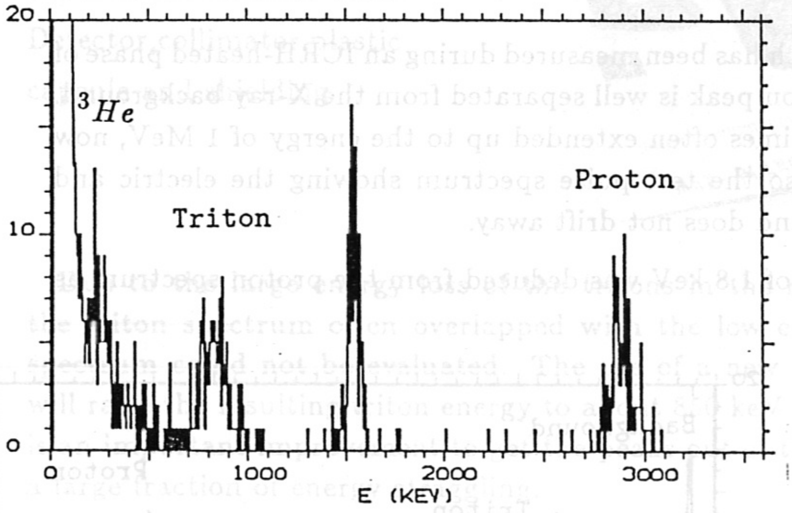

Fig.6:

Spectrum with an indication of ^3He (ASDEX # 22655)

5. References

{1} Bosch,H.-S.,Schumacher,U.:Measurements of Charged Fusion Products in ASDEX, Proc. of the 13th European Conference on controlled Fusion and Plasma Heating, Schliersee,1986,Vol.1,pp.124-127

{2} Lehner,G.,Pohl,F.:Reaktionsneutronen als Hilfsmittel der Plasmadiagnostik, Zeitschrift für Physik,207 (1967),83-104

{3} Stroth,U.:MULTRA-Code, to be published.

Advantages of a helium beam for active charge exchange diagnostics

W. Herrmann

Abstract

In charge exchange diagnostics, the application of a doping beam facilitates space-resolved measurements of the ion energy distribution and evaluation of the ion temperature. Hydrogen and helium beams are compared for their quality as doping beams for density and temperature profiles expected in ASDEX Upgrade with hydrogen and deuterium plasmas. The charge exchange cross-section of helium beams with 20 or 40 keV proves to be larger for a high energy of the analyzed particles than with hydrogen having an energy larger than 15 keV. As helium beams also penetrate better through the plasma, helium beams have distinct advantages for diagnostics of high-density, high-temperature plasmas. Estimates show that helium beams will allow measurement of neutral ion temperatures for densities as large as $1.5 \times 10^{14} cm^{-3}$. Further advantages of the helium beam are its small Halo effect (better space resolution) and the fact, that all the beam energy is concentrated in one component. The total beam power is less than for hydrogen beams with the same charge exchange rate.

Introduction

Active charge exchange diagnostics usually include a doping beam tailored to the special purpose of the diagnostics. These beams can and should then be optimized to yield best results. For ASDEX Upgrade it was found that the beam system should be capable of injecting protons, or He or hydrogen molecules, all with full energy. The following report gives the reasoning underlying the application of He beams.

Advantages of the Active System

Figure 1 summarizes the advantages of an active charge exchange system. For the localized neutral source in the case of a doping beam the radial integral in the expression for the flux reduces to a sum of the beam components. Instead of calculating the neutral density profile, one has to calculate the penetration η of the beam components to the volume investigated. This can be done if the density profile is known and if in a first estimate the ion temperature can be set equal to the electron temperature. (As the temperature has only a small effect on penetration, this approximation does not lead to a large error, especially if the beam energy is large compared with the plasma temperature.) With the same assumptions it is possible to determine the mean free path λ versus charge exchange of the analyzed particles. Here also the error introduced by setting $T_i = T_e$ is small, mainly when the high-energy part of the spectrum is investigated. With a knowledge of all energy-dependent functions one can determine the temperature in the usual way from the slope of the semilogarithmic plot of the corrected flux versus energy.

Disadvantages of a Hydrogen Beam

Figure 2 lists a few disadvantages of a hydrogen beam. The accuracy in determinating the energy depends on knowledge of the species mix, which is usually not very good. As many analyzers do not have a good mass resolution, the effective ionization and dissociation of molecular components may lead to a strong disturbance of the energy spectrum even in a deuterium plasma.

Hydrogen beams are known to have a large halo effect [1], which reduces the space resolution of the beam and may lead to a curved spectrum because the fluxes are now integrals of large areas with different temperatures. The high charge exchange rate at low energies, which causes the halo effect, is also the reason for the poor penetration of hydrogen beams.

Characteristics of a Helium Beam

Figure 3 shows the product of the charge exchange rate $\sigma \cdot v$ and the penetration η of He with 20 and 40 keV and hydrogen with 15 and 30 keV in a hydrogen plasma as a function of the energy of the detected particles [2]. Figure 4 shows the same for a deuterium plasma. (Density and temperature profiles expected for ASDEX Upgrade are used for calculating η. As the cross-section of the ASDEX Upgrade plasma is elliptic, the beam travels 0.65 m in the plasma to the centre.) The solid curves relate to zero density or $\eta = 1$. It can be seen, that for hydrogen and deuterium plasmas the charge exchange rate is small at low energies for He beams compared with that of hydrogen beams. This means that the halo effect will be very small for He beams. On the other hand it is clear that - at least for deuterium plasmas - low-energy hydrogen beams are a better source of charge exchange neutrals in the whole region where neutrals may be analyzed.

For a hydrogen plasma with very low density but high temperature, He beams might already be superior.

If the plasma density is increased - dotted curves or dotted curves with crosses - it becomes clear that He beams are more and more preferable. This is due to the penetration capability of He, which again is a result of the low charge exchange rate at low energies.

Figure 5 shows the penetration of hydrogen and helium beams in ASDEX Upgrade reference plasmas. (Only charge exchange and ionization are taken into account.) The good penetration of He and the minor effect of the plasma temperature can be seen (see also [3], [4]).

Summary - Advantages of a He beam

Figure 6 summarizes the advantages of the He beam. The He beam has only one energy component. The penetration of the beam does not have to be calculated for determination of the temperature. This reduces the possible errors in the calculation of the fluxes. As was shown, the halo effect is negligible with He beams with the result that the space resolution is as good as the dimensions of the beam allow. As only the full energy component of a hydrogen beam significantly contributes to the charge exchange rate because of the poor penetration of the lower energy components, the accelerated current can be reduced in a He beam, all the more so since, the density in the He beam with otherwise equal parameters is twice as large as in a hydrogen beam. This leads to a reduction in the power necessary for a helium beam.

The He beam is especially well suited to investigation of high-density and high-temperature plasmas. It may be possible to determine ion temperatures in ASDEX Upgrade for central densities as high as $1.5 - 2 \times 10^{14}\ cm^{-3}$.

References

[1] R.J. Goldston, Intern. School of Plasma Physics "Diagnostics for Fusion Reactor Condtions", Varenna, Italy, Sept. 1986, Vol. I, p. 263.

[2] R.C. Freeman, E.M. Jones, CLM-R 137, Culham 1974,
E.M. Jones, CLM-R 175, Culham 1977.

[3] V.V. Afrosimov, A.I. Kislyakov, see [1], p. 289.

[4] G.V. Roslyakov, see [1], p. 311.

Advantages of active charge exchange diagnostic

- space resolution
- external source of neutral particles
- (approximate) determination of the local ion energy distribution, if the T_e and n_e profiles and initial conditions of the beam are known:

The flux S of neutral particles is given by:

$$\frac{\Delta S(E)}{\sqrt{E \Delta E}} \sim \int_{-a}^{a} n_o(r) \cdot n_i(r) \frac{e^{-\frac{E}{Ti(r)}}}{T_i(r)^{3/2}} \cdot < \sigma_{cx}(v_{rel}) \cdot v_{rel} > e^{-\int_r^a \frac{ds}{\lambda(s,E)}} dr.$$

For active analysis this reduces to the sum of the beam components:

$$\frac{\Delta S(E)}{\sqrt{E \Delta E}} \sim \sum e^{-\frac{E}{T_i}} \frac{\eta \cdot n_o \cdot n_i}{T_i^{3/2}} \quad \sigma_{cx}(v_{rel}) \cdot v_{rel} e^{-\int_r^a \frac{ds}{\lambda(s,E)}} dr,$$

n_o: initial density of the beam

λ, η: mean free path and penetration from knowledge of $n_i(r)$ and $T_i(r) \approx T_e(r)$.

Determination of the ion temperature from the slope of the logarithmic plot of the flux versus energy:

$$\ell n \frac{\Delta S(E)}{f(E)\sqrt{E \Delta E}} \approx B - \frac{E}{T_i}.$$

Figure 1

Disadvantages of a hydrogen beam

- several energy components with not well-known distribution
  - ⇒ possible errors in determination of the flux
- molecular components
  - ⇒ effective source of high-energy neutrals disturbs flux spectra
- halo (low-energy neutrals from charge exchange with the beam produce cloud of neutral particles around the beam)
  - ⇒ reduction in space resolution
- high charge exchange rate at low energies
  - ⇒ bad penetration

Figure 2

Figure 3

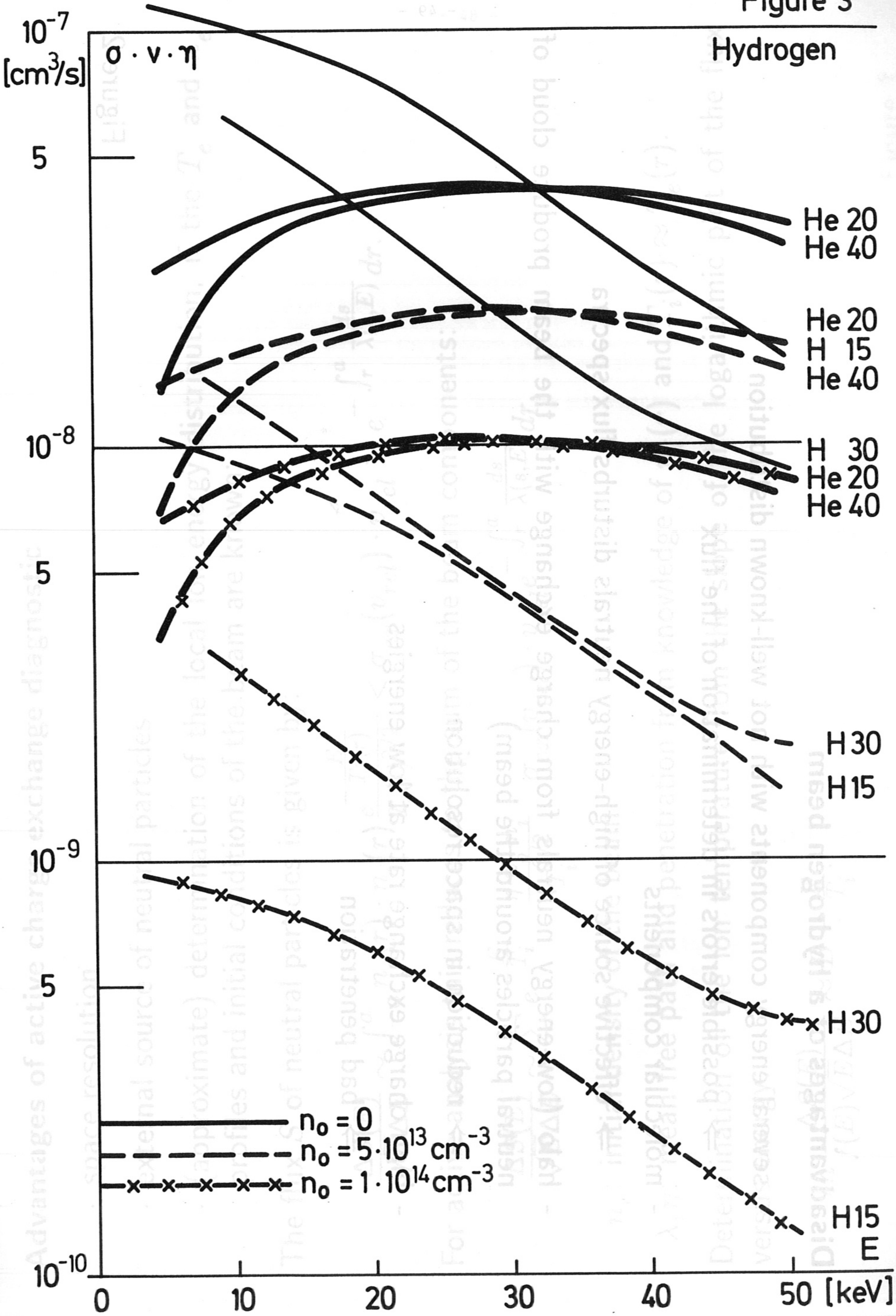
Hydrogen
σ · v · η
10^{-7} [cm³/s]
5
10^{-8}
5
10^{-9}
5
10^{-10}
He 20
He 40
He 20
H 15
He 40
H 30
He 20
He 40
H 30
H 15
H 30
H 15
E
$n_o = 0$
$n_o = 5 \cdot 10^{13}$ cm^{-3}
$n_o = 1 \cdot 10^{14}$ cm^{-3}
0
10
20
30
40
50 [keV]

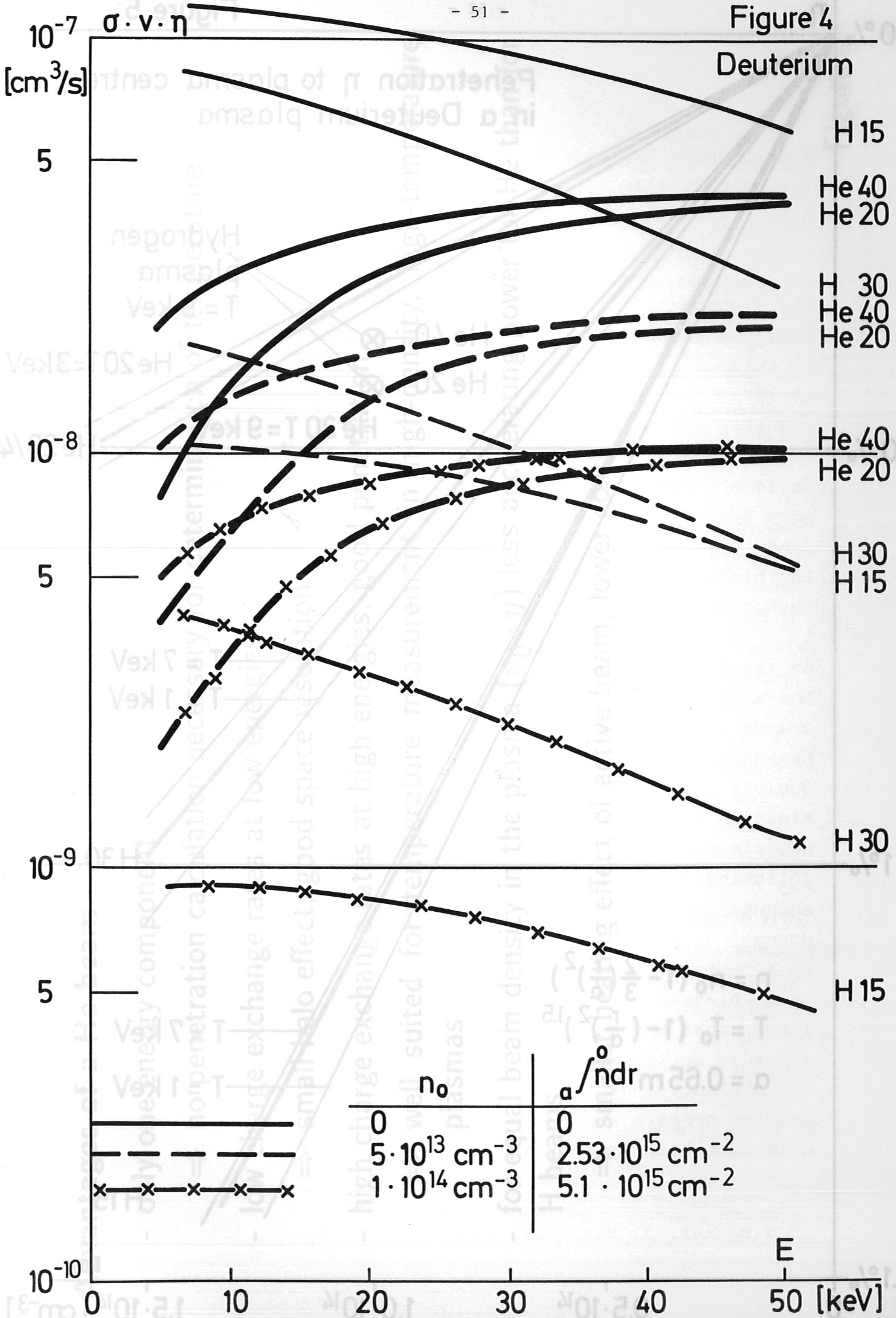

Figure 4

Deuterium
σ · v · η
[cm³/s]
10⁻⁷
5
10⁻⁸
5
10⁻⁹
5
10⁻¹⁰
H 15
He 40
He 20
H 30
He 40
He 20
He 40
He 20
H 30
H 15
H 30
H 15
n₀
$_a\int^0 n\,dr$
0
0
5 · 10¹³ cm⁻³
2.53 · 10¹⁵ cm⁻²
1 · 10¹⁴ cm⁻³
5.1 · 10¹⁵ cm⁻²
E
0
10
20
30
40
50
[keV]

Figure 5

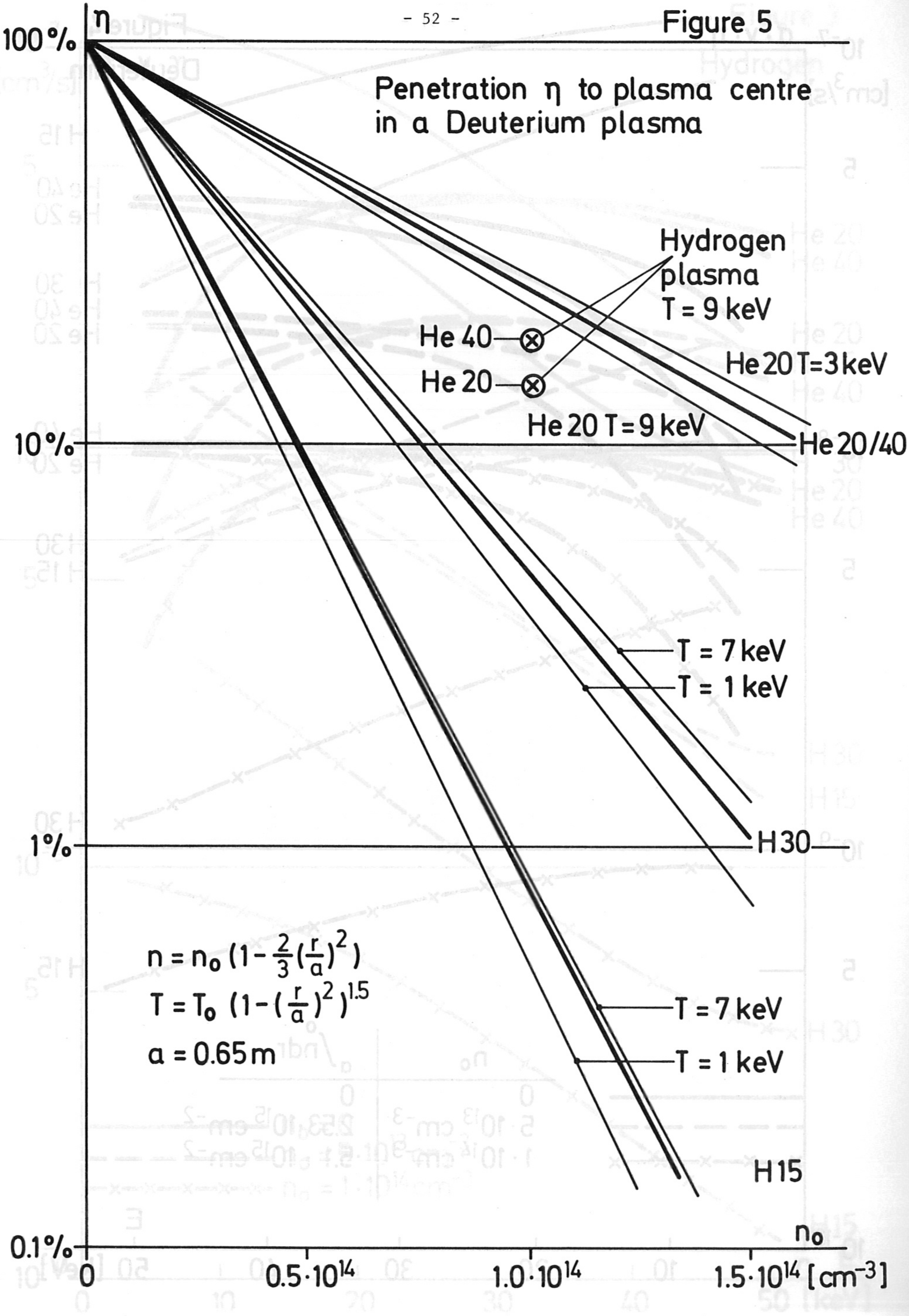

Penetration η to plasma centre in a Deuterium plasma

Advantages of a He beam

- only one energy component
  - ⇒ no penetration calculation necessary for determination of temperature
- low charge exchange rates at low energies
  - ⇒ small halo effect, good space resolution
- high charge exchange rates at high energies, good penetration
  - ⇒ well suited for temperature measurement in high-density, high-temperature plasmas
- for equal beam density in the plasma $(n_0 \cdot \eta)$ less accelerating power for He than for H beams
  - ⇒ smaller heating effect of active beam, lower costs

Figure 6

Simultaneous Background Measurement in the ASDEX Neutral Particle Diagnostics

H.-U. Fahrbach, H.M. Mayer

The diagnostic[1] measures the energy spectrum of the neutral particle flux leaving the plasma. The particles are detected by channeltrons after being electrically charged in the stripping cell and are separated in mass and energy by a magnetic and an electric field. Light, UV, neutrons and gammas create a background signal. The neutral spectrum steeply falls off towards higher energies and is therefore more and more buried in the background. To gain information from the inner parts of the plasma, the neutral particle fluxes at the highest possible energies have to be evaluated and the background has to be subtracted as accurately as possible.

In the past the background was determined by switching off the electrical field in the analyzer during a similar discharge recorded shortly before or after the discharge to be measured. Although ASDEX discharges are remarkably reproducible in many respects, improvement of background determination was desirable for several reasons: 1. The ASDEX experimental programme varies very fast. Identical discharges following one another are rare. Frequently parameters are scanned during series of discharges and the background may change. 2. Short-term phenomena (e.g. sawteeth) are not fixed to a certain time in the discharge. 3. During D°-NBI heating in D^+-plasmas the background was found to be up to 10 times larger than the neutral signal, thus preventing any evaluation. 4. It is anticipated that the running of the diagnostics and the evaluation of the data will be essentially automatic. The need to prepare and check comparison discharges is incompatible with automatic operation.

---

[1] F.Wagner, J. Vac. Sci. Technol., 20 (4), p. 1211-1217 (1982)

The principle of the new method is to chop the signal of all analyzer channels with a period shorter than the desired time resolution, normally 1 ms. This is done by a square function electric field in a condensor between the stripping cell and detector. During the first half-period the electric force prevents the charged particles from reaching the detectors, and only the background is measured. During the second half-period the field is zero and the sum of the signal and background is detected. The frequency and phase of the electric field are strictly coupled to those of the data acquisition system. Inspection and subtraction of the background are done by software.

It was possible to test the method under extreme conditions in ohmic discharges with an unusually high runaway level. During certain periods of the discharge the background level in one analyzer approached levels similar to D°-NI into a D^+ plasma. In Fig. 1 the corrected neutral particle flux spectra and spectra due to the background are shown. The background to the neutral particle signal ratio rapidly increases with energy. Near 4 keV it exceeds a factor of 10, near 7 keV a factor of 100. The corrected neutral flux spectrum appears to be essentially undistorted up to these H-values. This was verified by comparison with the second analyzer, which was exposed to much less runaway radiation.

Since the end of the summer shutdown of ASDEX this method of background correction has been routinely used in both analyzers. Even in discharges with moderate background the method turned out to be very advantageous, although half of the time is used for the measurement of the background. In the past the reliability of the measured fluxes at the critical energies was a question of reproducibility of the background. Now the statistical errors of the data provide a good quantitative measure for their reliability.

Fig. 1: Neutral particle flux spectra and background signal level simultaneously measured with the new system during ohmic discharges with high runaway radiation level.